Burns & Trauma, 2026, 14, tkag027
https://doi.org/10.1093/burnst/tkag027
Published: 1 April 2026
Research Article

OXFORD

Single-cell transcriptomic profiling identifies YY1 as a key regulator of fibroblast plasticity in hypertrophic scar formation

Qian Yu[1,§], Zonglin Huang[1,§], Lei Cai[2,§], Yanze Lv[3], Lianzhao Wang[4], Huanhuan Wu[4], Qiang Dai[1], Zikai Qiu[1], Zhigang Yang[1,‡,*], Xin Fu[1,‡,*], Ran Xiao[1,‡,*]

[1]Research Center of Plastic Surgery Hospital, Chinese Academy of Medical Sciences and Peking Union Medical College, 33 Ba-Da-Chu Road, Shijingshan District, Beijing, 100144, P.R. China
[2]Department of Fat Grafting and Body Contouring of Plastic Surgery Hospital, Chinese Academy of Medical Sciences and Peking Union Medical College, 33 Ba-Da-Chu Road, Shijingshan District, Beijing, 100144, P.R. China
[3]Department of Hemangioma and Vascular Malformation of Plastic Surgery Hospital, Chinese Academy of Medical Sciences and Peking Union Medical College, 33 Ba-Da-Chu Road, Shijingshan District, Beijing, 100144, P.R. China
[4]Comprehensive Treatment Center of Scar of Plastic Surgery Hospital, Chinese Academy of Medical Sciences and Peking Union Medical College, 33 Ba-Da-Chu Road, Shijingshan District, Beijing, 100144, P.R. China

[*]Corresponding authors. Zhigang Yang, E-mail: yangzg@psh.pumc.edu.cn; Xin Fu, E-mail: fuxin@psh.pumc.edu.cn; Ran Xiao . E-mail: xiaoran@psh.pumc.edu.cn
[‡]Ran Xiao, Xin Fu, and Zhigang Yang have contributed equally to this work as co-corresponding authors.
[§]Qian Yu, Zonglin Huang, and Lei Cai have contributed equally to this work as co-first authors.

Abstract

Background: **Hypertrophic scars (HTSs) are characterized by excessive extracellular matrix deposition and impaired scar remodelling. Fibroblasts are central to HTS pathogenesis, yet clinical strategies remain limited by an incomplete understanding of fibroblast heterogeneity and transcriptional regulation. This study aimed to identify a key fibroblast subpopulation and its regulatory transcription factors to address this translational gap.**

Methods: **Single-cell RNA sequencing was performed on dermal cells from freshly excised human HTS and normal skin (NS) tissues. Fibroblast subsets and transcriptional regulators were identified using Seurat, pseudotime, transcription factor prediction, and cell–cell communication analyses. Functional validation involved lentiviral overexpression of Yin Yang 1 (YY1) in fibroblasts derived from patients with hypertrophic scars, followed by bulk RNA sequencing, western blotting, CUT&Tag, and immunofluorescence assays.**

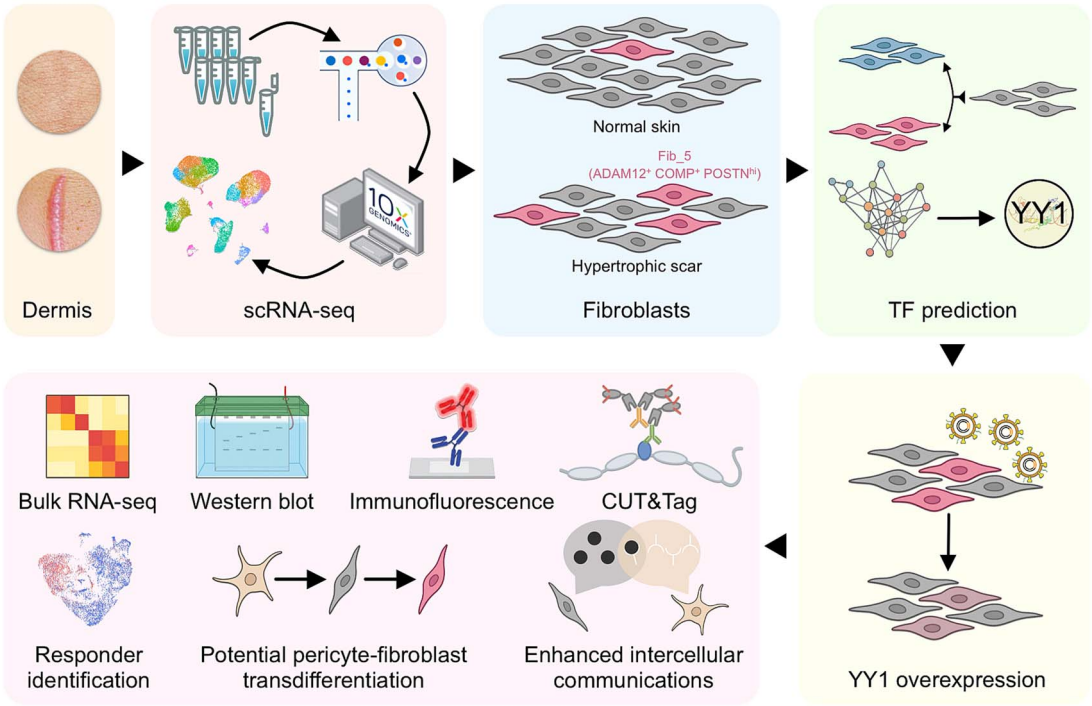
Results: **Clinical HTS specimens showed characteristic collagen overproduction and vascular hyperplasia. Single-cell analysis of 43 303 cells revealed disease-specific shifts in cellular composition, including pronounced pericyte expansion and reduced fibroblast abundance. Notably, fibroblast subcluster Fib_5 (ADAM12^{+} COMP^{+} POSTN^{hi}) increased despite the overall fibroblast decline in HTS and exhibited upregulated fibrotic gene expression. Cross-validation using combined public datasets comprising 21 samples indicated that the Fib_5-like subcluster is conserved across fibrotic conditions. Pseudotime analyses placed Fib_5 within an HTS-dominant branch, State 6; transcription factor prediction from branch-dependent differentially expressed genes identified YY1 as the only predicted transcription factor also differentially expressed in State 6. Functional validation showed that YY1 overexpression in fibroblasts derived from patients with HTS reversed fibrotic gene expression profiles, with Fib_5 identified as a primary responder by Scissor. CUT&Tag analysis validated these findings at the epigenomic level. Cell–cell communication analyses further revealed marked reprogramming of fibroblast-pericyte signalling across multiple fibrosis-related pathways in HTS.**

Conclusion: **This work establishes the Fib_5-YY1 axis as a central hub in HTS pathogenesis, with YY1-mediated fibroblast plasticity as a key transcriptional mechanism underlying skin fibrogenesis.**

Received: 10 November 2025. **Revised:** 27 March 2026. **Accepted:** 30 March 2026
© The Author(s) 2026. Published by Oxford University Press.
This is an Open Access article distributed under the terms of the Creative Commons Attribution-NonCommercial License (https://creativecommons.org/licenses/by-nc/4.0/), which permits non-commercial re-use, distribution, and reproduction in any medium, provided the original work is properly cited. For commercial re-use, please contact reprints@oup.com for reprints and translation rights for reprints. All other permissions can be obtained through our RightsLink service via the Permissions link on the article page on our site—for further information please contact journals.permissions@oup.com.

Downloaded from academic.oup.com/burnstrauma/article/doi/10.1093/burnst/tkag027/8571429 by guest on 12 October 2026

Graphical abstract



Keywords Single-cell RNA sequencing, Hypertrophic scar, Fibroblast plasticity, Transcription factor, Yin Yang 1, Fibrosis, Extracellular matrix

Highlights

- **We identified a counter-trend expansion of a fibroblast subpopulation (Fib_5: ADAM12^{+} COMP^{+} POSTN^{hi}) exhibiting a markedly fibrogenic phenotype in hypertrophic scars (HTSs), consistent with conserved pro-fibrotic cellular states observed in other fibrotic skin disorders.**
- **Our findings demonstrated that YY1 downregulation exerts pro-fibrotic effects in HTS fibroblasts, while its overexpression attenuates fibrogenic activation, highlighting YY1 as a key transcriptional regulator of fibroblast fibrotic programs.**
- **We revealed significant changes in fibroblast–pericyte signalling in HTS, which was associated with multiple fibrosis-related pathways through cell–cell communication analyses.**

Background

Hypertrophic scars (HTSs) are pathological outcomes of aberrant wound healing, characterized by excessive extracellular matrix (ECM) deposition and persistent myofibroblast activation, leading to disfigurement, pruritus, and functional impairment that severely affect quality of life. Fibroblasts, particularly myofibroblasts, are widely recognized as central mediators of scar formation [1]; however, current antifibrotic therapies targeting these cells have limited efficacy because of an incomplete understanding of their heterogeneity [2–4]. Recent studies indicate that fibroblasts in scars may arise not only locally but also from pericytes or through endothelial-to-mesenchymal transition [5–8], underscoring the need for subtype-specific therapeutic strategies.

Single-cell RNA sequencing (scRNA-seq) has transformed the analysis of fibroblast heterogeneity in HTS. Although previous studies identified disease-specific subsets [9–13], key gaps remain in identifying master transcriptional regulators amenable to pharmacological modulation. Notably, transcription factors (TFs) such as ETV4, TWIST2, and CREB1 drive fibrotic reprogramming [10, 14, 15], yet effective TF-targeted therapies for HTS remain elusive, underscoring the need for new approaches.

In this study, we generated a high-resolution cellular atlas of dermal tissues from normal skin (NS) and HTS using scRNA-seq. We sought to identify a key fibroblast subcluster and define the role of its regulatory TFs in modulating the fibrotic phenotype of HTS fibroblasts. By examining fibroblast heterogeneity and transcriptional regulation, this study provides insight into the mechanisms underlying HTS pathology, prioritizes candidate regulatory programmes for further mechanistic investigation, and expands the dermal scRNA-seq resource for future studies.

Methods

Collection of normal and hypertrophic scar skin samples

NS samples for the control group were obtained from patients undergoing abdominal plastic surgery or breast reduction surgery. HTS tissue samples were obtained from patients undergoing scar

Downloaded from academic.oup.com/burnstrauma/article/doi/10.1093/burnst/tkag027/8571429 by guest on 12 October 2026

Table 1 Clinical and demographic details of the patients

Sample name	Group	Age	Sex	Collection site	Post-trauma	Scarring time
CON0514	NS	45	Male	Abdomen		
CON0517	NS	25	Female	Breast		
CON0715	NS	18	Female	Breast		
SC1	HTS	44	Female	Upper arm	Scald	3 years
DIS0129	HTS	16	Male	Thigh	Burn	4 years
DIS0201	HTS	20	Male	Breast	Scald	19 years
DIS0306	HTS	8	Female	Breast	Burn	5 years

excision; the scars were prominently raised above the skin surface, located on the trunk or limbs, had been present for at least 1 year, and had received no prior treatment. In total, seven patients were included in this study; additional clinical and demographic details are provided in Table 1. The study was approved by the Ethics Committee of the Plastic Surgery Hospital, Chinese Academy of Medical Sciences and Peking Union Medical College (approval number, 2021(179)). Informed consent was obtained from all patients before surgery.

Single-cell RNA sequencing

Preparation of dermal single-cell suspension

Freshly excised NS and hypertrophic scar tissues were rinsed twice with sterile Dulbecco's phosphate-buffered saline (DPBS; Solarbio, China), cut into thin strips $\sim 0.1 \times 1$ cm in size, and placed in 0.25% dispase II solution (Sigma, USA) for 2 h at 37°C. After incubation, the tissues were removed, the dermis was separated from the epidermis, and the dermal tissue was minced. The minced dermal tissue was then added to 30 ml of enzyme digestion solution containing 0.2% type I collagenase solution (Sigma) and 60 U/ml DNase I (Sigma, then placed on a shaker at 100 rpm and 37°C for 2 h. The digested tissue was filtered through a 40 μm cell strainer (BD, USA), and the filtrate was centrifuged at 300 g and 4°C for 5 min. After the supernatant was discarded, 1–5 ml of red blood cell lysis solution was added to the pellet, which was placed on ice for 4 min, followed by centrifugation at 300 g and 4°C for 5 min. The cells were rinsed twice with ice-cold DPBS and centrifuged again at 300 g and 4°C for another 5 min. After discarding the supernatant, the cells were resuspended in 0.4% bovine serum albumin (BSA)–phosphate-buffered saline (PBS), and the cell concentration was adjusted to $(0.8–1.2) \times 10^6$/ml; the cell suspension was then placed on ice. Cell counting and morphological assessment were performed under a light microscope after mixing the cell suspension with trypan blue.

Single-cell transcriptome library construction and sequencing

Single-cell complementary DNA (cDNA) library preparation and sequencing were performed by Novogene (Beijing, China). The 10x Genomics Chromium platform was used; Chromium Single Cell 3′ Library & Gel Bead Kit v3 and Chromium Single Cell 3′ Chip Kit v3 were used for single-cell partitioning; and Illumina NovaSeq 6000 was used for sequencing. Single-cell suspensions with the required cell viability ($\geq$80%) were combined with enzymes and barcode-carrying gel beads, then encapsulated in oil droplets within the microfluidic device to form Gel bead-in-Emulsion (GEM) structures. Effective GEMs contained a single cell, MasterMix, and gel bead containing pre-loaded 10$\times$ primers, where cell lysis and reverse transcription occurred. Library construction was initiated after cDNA amplification passed quality control. After library preparation and quality control were completed, RNA-sequencing was performed using the Illumina NovaSeq 6000 platform.

Single-cell data processing and analysis

Raw data processing

Raw FASTQ files were processed using Cell Ranger version 3.0.0. Sequencing reads were first aligned to a predefined reference genome for unique molecular identifier (UMI) counting and generation of a UMI count matrix for each gene in each cell. Data filtering was performed using the following parameters: a maximum mitochondrial gene proportion of 30%, a maximum red blood cell gene proportion of 5%, and gene counts ranging from 200 to 8000, with genes expressed in fewer than three cells excluded. Finally, doublets were removed using the R package DoubletFinder version 2.0.2 [16].

Cell clustering and annotation

Unsupervised clustering was performed using Seurat version 3.1.5 [17], and batch effects were corrected by canonical correlation analysis; the results were visualized using Uniform Manifold Approximation and Projection (UMAP). The resolution was tested incrementally from 0.2 to 0.8 in steps of 0.05 and selected using cluster expression heatmaps. The FindAllMarkers function was used for differentially expressed gene (DEG) analysis, and cell types were manually annotated based on the expression of marker genes identified in previous studies. Subsequently, the FindVariableFeatures function was used to identify variable genes, and Spearman's rank correlation coefficient was used to assess correlations among different cell types or subclusters.

Advanced analyses

The R package clusterProfiler [18] was used for Gene Ontology and Kyoto Encyclopedia of Genes and Genomes pathway enrichment analyses. For intergroup DEGs, the online tool Metascape [19] was used. Pseudotime trajectory analysis was then performed separately on the whole dataset and the fibroblast subset using the R package monocle3 version 0.2.1 [20]. Variable genes identified

Downloaded from academic.oup.com/burnstrauma/article/doi/10.1093/burnst/tkag027/8571429 by guest on 12 October 2026

by Seurat were used to construct pseudotime trajectories, followed by branched expression analysis modelling to detect highly variable genes at branch points and branch-specific DEGs. The TRRUST v2 database [21] was then used to predict TFs from the DEGs identified in the previous step. Using the Scissor package [22] (version 2.1.0), the scRNA-seq data were integrated with the bulk RNA-sequencing (bulk-seq) results to identify fibroblast subpopulations associated with the phenotype induced by Yin Yang 1 (YY1) overexpression, following the steps described in the package tutorial. The selection results were then added to the Seurat object metadata for subsequent visualization and DEG analyses using the methods described above. The CellChat package [23] (version 2.1.2) was used to identify and visualize significant cell–cell communication networks between fibroblast subclusters and pericytes. Pathway centrality scores were calculated using the built-in functions.

Validation of publicly available data

Public datasets from the National Center of Biotechnology Information (NCBI) Gene Expression Omnibus database (https://www.ncbi.nlm.nih.gov/geo/) were used to cross-validate the preliminary findings. For the NS group, five samples were obtained from GSE130973 [24], five from GSE151177 [25], three from GSE156326 [26], and one from GSE181316 [27], totalling 14 NS samples. For the HTS group, three samples were obtained from GSE156326 [26], three from GSE181316 [27], and one from GSE243716, totalling seven HTS samples. Following dataset integration and batch correction, unsupervised clustering and cell type annotation were performed as described above. For correlation analyses, the average log-normalized expression of the subclusters of interest was used to compute and visualize Pearson's r.

Overexpression of YY1 in hypertrophic scar fibroblasts

YY1-overexpressing plasmid construction and amplification

The coding sequence of the human YY1 gene (Gene ID: 7528) was first obtained from the NCBI website. Restriction sites within the sequence were then identified and matched to those in the pCDH-CMV-MCS-EF1-CopGFP plasmid to select suitable sites. Construction of the target plasmid was commissioned to Tsingke (Beijing, China). Briefly, the plasmid was digested with restriction enzymes at the selected sites, followed by confirmation by agarose gel electrophoresis. The YY1-overexpressing plasmid was then introduced by heat shock transformation, and monoclonal positive strains were selected for amplification to obtain a sufficient amount of plasmid. Plasmid extraction was performed using the EndoFree Plasmid Maxi Kit (Qiagen, Germany) according to the manufacturer's instructions. Finally, plasmid concentration was measured with a UV-Vis spectrophotometer (NanoDrop, USA), and the solution was stored at -20°C for subsequent experiments.

Lentivirus packaging

HEK 293 T cells were cultured in high-glucose Dulbecco's modified Eagle's medium (DMEM; Gibco, USA) supplemented with 10% foetal bovine serum (FBS; Gibco), as described for fibroblast culture. When the cells reached 80% confluence, transfection was performed using jetPRIME transfection reagent (Polyplus, France) according to the manufacturer's instructions. The transfection mixture contained 5 μg target plasmid, 3.75 μg psPAX2 plasmid, and 1.25 μg of pMD2.G plasmid. Viral supernatants were collected at 24, 48, and 72 h after transfection. The supernatants were centrifuged at 200 g for 5 min to remove precipitates, and cell debris and impurities were removed using a 0.45 μm syringe filter (Millipore, USA). The collected lentiviral supernatants were then ultracentrifuged at 22 500 rpm (P70AT-1584 rotor, Himac, Japan) for 3 h. After the supernatant was discarded, the lentiviral pellet at the bottom of the ultracentrifuge tube was resuspended in low-glucose DMEM (Gibco) and stored at 4°C for subsequent experiments or at -80°C for long-term storage.

Isolation and transduction of hypertrophic scar fibroblasts

To isolate fibroblasts from HTS, scar tissue was first prepared using the method described above. When the cells reached 70% confluence, lentiviral suspension and 10 μg/ml polybrene reagent (Millipore) were added to the medium for transduction. After 18–24 h, the medium was replaced with fresh complete medium, and the cells were cultured for a further 48 h, after which RNA and protein were collected for subsequent experiments. The remaining cells were cryopreserved for future use.

Gene expression difference evaluation with RNA sequencing

RNA from YY1-overexpressing HTS fibroblasts was extracted using TRIzol reagent (Sigma). Library construction and sequencing were again performed by Novogene. RNA integrity was first assessed using the 2100 Bioanalyzer system (Agilent, USA) in combination with the RNA 6000 Nano Kit (Agilent). Raw sequencing data were quality-checked using FastQC, and low-quality reads were removed by Next Generation Sequencing Quality Control (NGSQC) procedures. FPKM values, defined as fragments per kilobase of exon per million mapped fragments, were calculated using StringTie. After filtering with the set threshold ($|\log2FC| \geq 1$, adjusted P-value ≤ 0.05), DEGs were analysed using the R packages DESeq2 version 1.20.0 [28] and edgeR version 3.22.5 [29].

Protein expression evaluation by western blot

According to the manufacturer's instructions, protease inhibitor cocktail (Beyotime, China) and phosphatase inhibitor cocktail (Beyotime) were added to RIPA lysis buffer (Beyotime) for protein extraction. All procedures were performed at low temperature to minimize protein degradation. After extraction, protein concentration was determined using the BCA Protein Assay Kit (Beyotime); absorbance was measured using a multimode microplate reader (Perkin Elmer, USA) at 562 nm, and concentrations were calculated using the standard curve. Protein samples were then separated by Sodium Dodecyl Sulfate – Polyacrylamide Gel Electrophoresis (SDS-PAGE) and transferred to Polyvinylidene Fluoride (PVDF) membranes (Millipore) using a wet transfer system. The membranes were blocked in Tris-Buffered Saline with Tween 20 (TBST, Applygen, China) containing 5% skim milk (Fujifilm, Japan) on a shaker at room temperature for 1 h.

Downloaded from academic.oup.com/burnstrauma/article/doi/10.1093/burnst/tkag027/8571429 by guest on 12 October 2026

The PVDF membranes were incubated overnight at 4°C with diluted primary antibodies: Anti-Glyceraldehyde-3-phosphate dehydrogenase (GAPDH, 1:25000, HRP-60004, Proteintech, USA), Anti-YY1 (1:500, sc-7341, Santa Cruz, USA), Anti-COL1 (1:2000, 14 695-1-AP, Proteintech), Anti-COL3 (1:500, 22 734-1-AP, Proteintech), Anti-FN1 (1:20000, 15 613-1-AP, Proteintech), Anti-AKT (1:25000, 60 203-2-Ig, Proteintech), and Anti-pAKT (Ser473; 1:5000, 66 444-1-Ig, Proteintech). Following incubation, the membranes were incubated with the corresponding secondary antibodies at room temperature for 1 h; specifically, goat anti-rabbit (1:3000, ab6721, Abcam, UK) was used for anti-COL1, anti-COL3, and anti-FN1, while goat anti-mouse (1:5000, ab6789, Abcam) was used for anti-GAPDH, anti-YY1, anti-AKT, and anti-pAKT. Finally, protein expression was visualized using the ECL Chemiluminescent Substrate Reagent Kit (Invitrogen, USA). Band intensities were quantified using ImageJ software (version 2.14.0). Protein expression levels were converted to greyscale values and normalized to GAPDH as the internal control. For intergroup comparisons, the normalized values were further scaled to the mean expression level of the NS group or PCDH control group. Statistical analyses and graphs were generated using GraphPad Prism (version 10.1.1).

Immunofluorescence staining

Frozen sections were first equilibrated to room temperature for 15 min and washed three times with PBS (Solarbio) for 5 min each. The sections were then permeabilized with 0.1% Triton X-100 (Solarbio) at room temperature for 20 min, washed three times with PBS, and blocked with 10% goat serum (Gibco) at room temperature for 1 h. The sections were then incubated overnight at 4°C in a humidified chamber with primary antibodies diluted in 1% BSA (Invitrogen), including anti-YY1 (1:250, sc-7341, Santa Cruz), anti-COL1 (1:500, 14 695-1-AP, Proteintech), anti-COL3 (1:500, 22 734-1-AP, Proteintech), anti-FN1 (1:200, 15 613-1-AP, Proteintech), and anti-RGS5 (1:100, ab138019, Abcam). Secondary antibodies were also diluted in 1% BSA and incubated with the sections in the dark at 37°C for 1 h. Specifically, Alexa Fluor 647 Goat Anti-Rabbit (1:500, ab150079, Abcam) was used for anti-COL1, anti-COL3, anti-FN1, and anti-RGS5, while Alexa Fluor 647 Goat Anti-Mouse (1:500, ab150115, Abcam) was used for anti-YY1. The sections were then incubated with 4′,6-diamidino-2-phenylindole (DAPI) for 7 min in the dark at room temperature, mounted with antifade reagent (Invitrogen), and cover-slipped. Images were acquired using a confocal microscope (SP8, Leica, Germany). Immunofluorescence signal quantification was performed using ImageJ. The fluorescence intensity of target proteins was normalized to the DAPI signal to account for variation in cell number. The normalized values were further scaled to the mean fluorescence intensity of the PCDH control group. Quantitative analyses and data visualization were performed using GraphPad Prism.

Additionally, for immunofluorescence staining of YY1-overexpressing HTS fibroblasts, cells infected with the target lentivirus were seeded onto glass slides (Solarbio) placed in the bottom of a six-well plate. After cell attachment was confirmed microscopically, the slides were removed and washed twice with PBS, followed by fixation with 4% paraformaldehyde (Sigma) for 10 min. The remaining steps were the same as those described above.

CUT&Tag sequencing

Cell line culture

The BJ human foreskin fibroblast cell line (CXH00618) was obtained from Wuhan EnkiLife Biotech Co., Ltd. Cells were cultured in high-glucose DMEM (Gibco) supplemented with 10% FBS (Gibco) and 1% penicillin–streptomycin (Gibco) at 37°C in a humidified atmosphere containing 5% CO_2. Cells were passaged at 80%–90% confluence using 0.25% trypsin.

Cell preparation and YY1 modulation

BJ fibroblasts were divided into three groups: a YY1-overexpressing group transduced with the YY1-carrying lentivirus as described above, a YY1-knockdown group transfected with a YY1-targeting small interfering RNA (sense: 5′-CGACGACUACA UUGAACAA(dT)(dT)-3′, antisense: 5′-UUGUUCAAUGUAGUCGU CG(dT)(dT)-3′; high-performance liquid chromatography–purified, Tsingke, China) using Lipofectamine 3000 (Invitrogen) according to the manufacturer's instructions, and an untreated control group. Overexpression and knockdown efficiency were verified by quantitative real-time Polymerase Chain Reaction (PCR) using the following primers: YY1-F, 5′-GTTCAGGGATAACTCGGCCA-3′; YY1-R, 5′-TTCGAACGTGCACTGAAAGG-3′.

Library construction, sequencing, and data processing

Library construction and sequencing were again performed by Novogene following the protocol of Kaya-Okur *et al.* [30], using anti-YY1 (sc-7341 X, Santa Cruz). Libraries were sequenced on the Illumina NovaSeq platform, generating 150 bp paired-end reads. Raw reads were quality filtered with fastp (version 0.20.0) [31], aligned to the human reference genome using BWA (version 0.7.12) [32], and filtered for uniquely mapped reads (MAPQ $\geq$13). Peaks were called with MACS2 (version 2.1.0) [33] (q-value <0.05), and motif discovery was performed using HOMER (version 4.9.1) [34]. Peak annotation was conducted using ChIPseeker [35]. For differential peak analysis, peaks were merged with BEDTools [36], and those with an RPM fold change >2 were considered differential. Genome browser tracks were visualized using Integrative Genomics Viewer (IGV, version 2.19.7).

Statistical analysis

Data are presented as mean $\pm$ standard deviations. Statistical analyses were performed using R (version 4.2.0), GraphPad Prism (version 10.1.1), and the corresponding packages described above. All statistical tests were two-sided, and a P-value < 0.05 was considered statistically significant. For scRNA-seq data, DEGs were identified using the Seurat package (version 4.4.0), with fold change thresholds tailored to each analysis as detailed in the relevant sections. For bulk RNA-seq data, DEGs were identified using DESeq2 (version 1.20.0) and edgeR (version 3.22.5), using thresholds of $|\log_2 FC| \geq 1$ and adjusted P-value ≤ 0.05. Multiple testing correction was performed using the Benjamini–Hochberg method where applicable. Spearman's rank correlation was used for within-dataset cell-type comparisons, whereas Pearson's correlation was used for cross-dataset expression comparisons. Western blot band intensities and immunofluorescence signals were quantified using ImageJ (version 2.14.0), normalized as described above, and compared between groups using unpaired two-tailed t-tests.

Downloaded from academic.oup.com/burnstrauma/article/doi/10.1093/burnst/tkag027/8571429 by guest on 12 October 2026

Results

Comparative analysis of dermal cell composition between normal skin and hypertrophic scar

After raw-data processing and filtering, 43 303 high-quality cells were retained, including 18 137 from the NS cohort and 25 166 from the HTS cohort. Following sample integration, clustering and visualization using UMAP showed that dermal tissue could be classified into 21 distinct cell clusters (c0–c20), which were annotated into nine cell types: vascular endothelial cells, pericytes, fibroblasts, T cells, mast cells, dendritic cells, lymphatic endothelial cells, Schwann cells, and keratinocytes, each with distinct transcriptional patterns (Figure 1b–d). As shown in the stacked percentage plot (Figure 1e), a significant shift in cell-type distribution between the NS and HTS groups was evident. Notably, pericytes showed the greatest increase in HTS

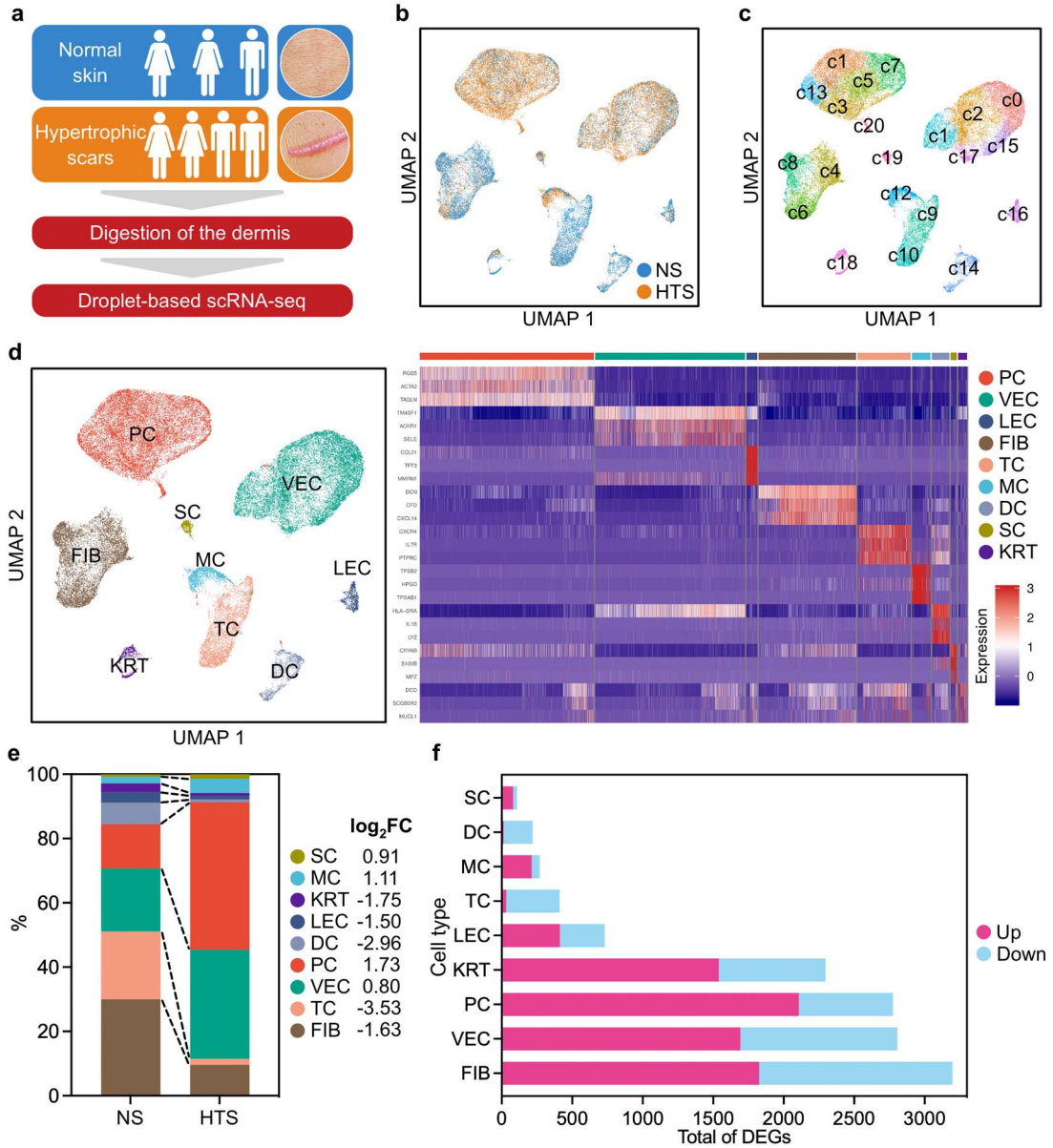


Figure 1 Overview of single-cell RNA sequencing results. (**a**) Schematic overview of patient sampling and the sequencing workflow. (**b**–**d**) UMAP visualization of the data after dimensionality reduction and clustering, with cells coloured by group (b), separated into 21 clusters (c), and annotated into nine cell types with distinct transcriptional characteristics (d). (**e**) Stacked percentage bar charts showing changes in the proportions of different cell types in the dermis of NS and HTS, with the greatest increase in pericytes ($log_2FC = 1.73$) and the greatest decrease in T cells ($log_2FC = -3.53$). (**f**) Stacked bar charts showing the total number of DEGs ($|log_2FC| > 0$, adjusted P value <0.05) by cell type, with red bars indicating upregulated DEGs and bluebars indicating downregulated DEGs. Fibroblasts show the highest total number of DEGs, indicating a marked shift in biological function in HTS. *UMAP* Uniform Manifold Approximation and Projection, *NS* normal skin, *HTS* hypertrophic scars, *PCs* pericytes, *VECs* vascular endothelial cells, *LECs* lymphatic endothelial cells, *FIBs* fibroblasts, *TCs* T cells, *MCs* mast cells, *DCs* dendritic cells, *SCs* Schwann cells, *KRTs* keratinocytes, *DEGs* differentially expressed genes

Downloaded from academic.oup.com/burnstrauma/article/doi/10.1093/burnst/tkag027/8571429 by guest on 12 October 2026

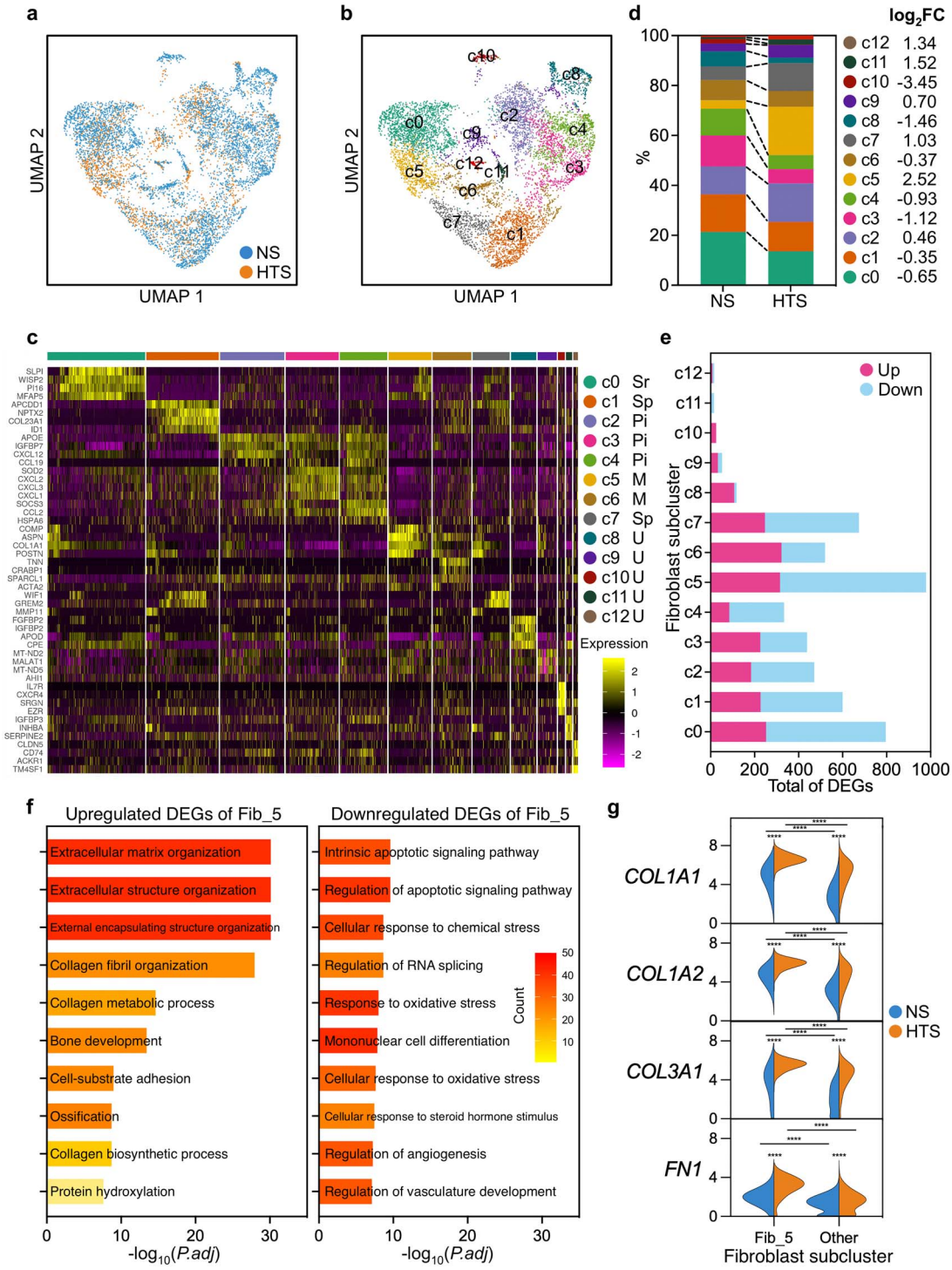


Figure 2 Selective increase of the subcluster Fib_5 and its fibrotic phenotype. (**a**, **b**) UMAP visualization of fibroblasts coloured by group (a) and reclustered into 13 subclusters by unsupervised clustering (b). (**c**) Transcriptional heatmap showing distinct transcriptomic patterns across subclusters. (**d**) Stacked percentage plot showing differences in the proportions of fibroblast subclusters between NS and HTS; abbreviations for fibroblast subtypes are shown after the subcluster legend. (**e**) Stacked bar charts showing the total number of DEGs ($|\log_2 FC| > 0.25$, adjusted *P* value < 0.05) by subcluster, with red bars indicating upregulated DEGs and blue bars indicating downregulated DEGs; Fib_5 (c5) shows the highest total number of DEGs. (**f**) Bar plots showing GO biological process enrichment of filtered upregulated (left) and downregulated (right) DEGs in Fib_5. (**g**) Split violin plots showing intergroup comparisons of selected fibrotic gene expression in Fib_5 versus all other subclusters; statistical significance was assessed using the Wilcoxon rank-sum test. $^{****}P < 0.0001$. *GO* Gene Ontology, *Sr* secretory-reticular fibroblasts, *Sp* secretory-papillary fibroblasts, *Pi* pro-inflammatory fibroblasts, *M* mesenchymal fibroblasts, *U* unidentified fibroblasts, *UMAP* Uniform Manifold Approximation and Projection, *NS* normal skin, *HTS* hypertrophic scars

Downloaded from academic.oup.com/burnstrauma/article/doi/10.1093/burnst/tkag027/8571429 by guest on 12 October 2026

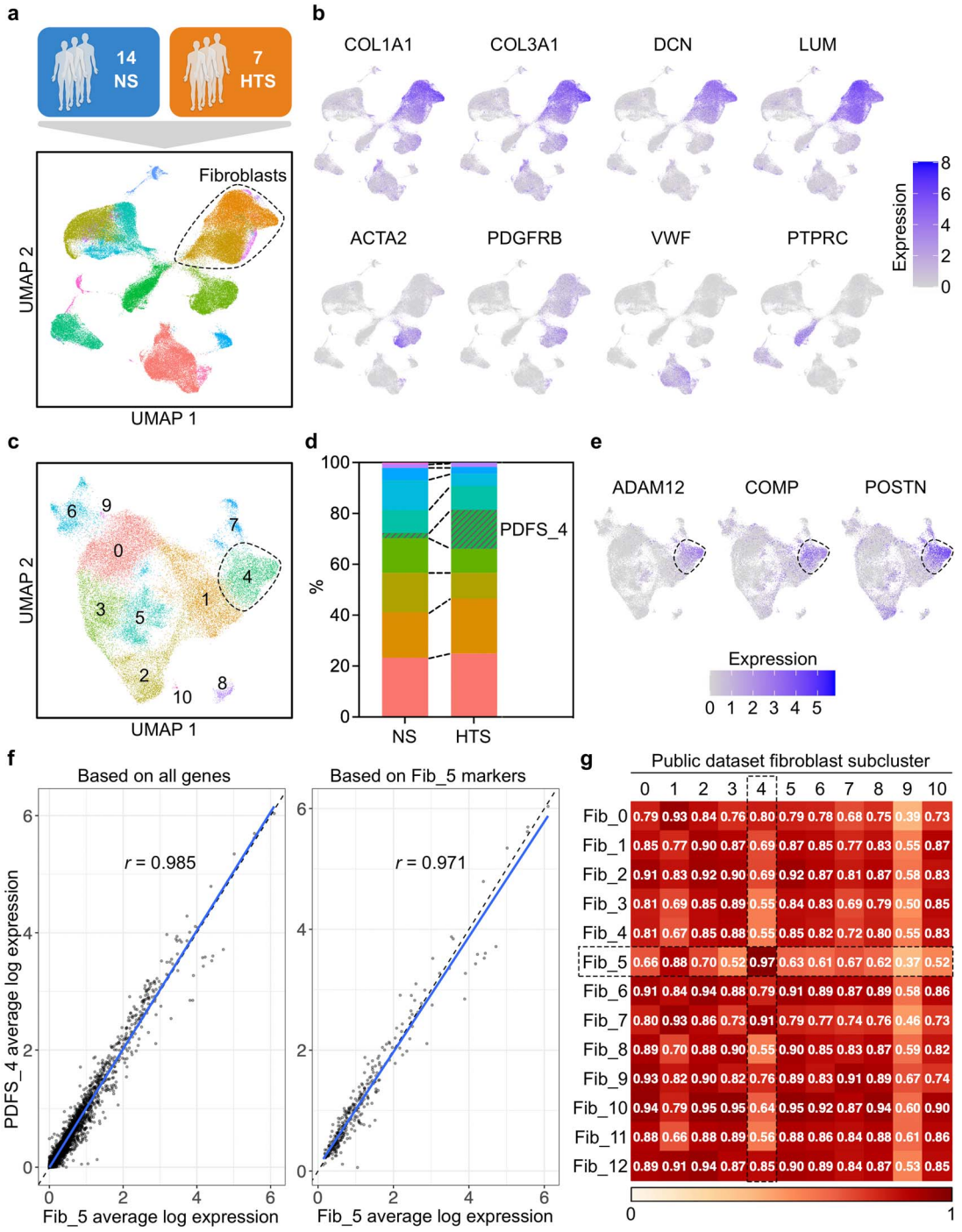


Figure 3 Cross-validation using public datasets. (**a**) Overall, 14 NS and 7 HTS publicly available samples were used to generate the combined dataset, visualized by UMAP (lower). (**b**) Feature plots of selected genes for fibroblast identification. (**c**) UMAP visualization of subset fibroblasts, separated into 11 subclusters and coloured accordingly. (**d**) Stacked percentage bar chart showing shifts in the proportions of different subclusters between the NS and HTS groups, with public dataset fibroblast subcluster_4 (PDFS_4, striped in the figure) showing the most marked expansion in HTS. (**e**) Feature plots of subset fibroblasts coloured by the expression of marker genes previously identified for Fib_5. (**f**) Correlation scatter plots of the average log-normalized expression of Fib_5 and PDFS_4 based on all genes (left) and Fib_5 marker genes (right). (**g**) Heatmap showing cluster-to-cluster correlation between the fibroblast subset in the present study and that in the public datasets. *UMAP* Uniform Manifold Approximation and Projection, *NS* normal skin, *HTS* hypertrophic scars

Downloaded from academic.oup.com/burnstrauma/article/doi/10.1093/burnst/tkag027/8571429 by guest on 12 October 2026

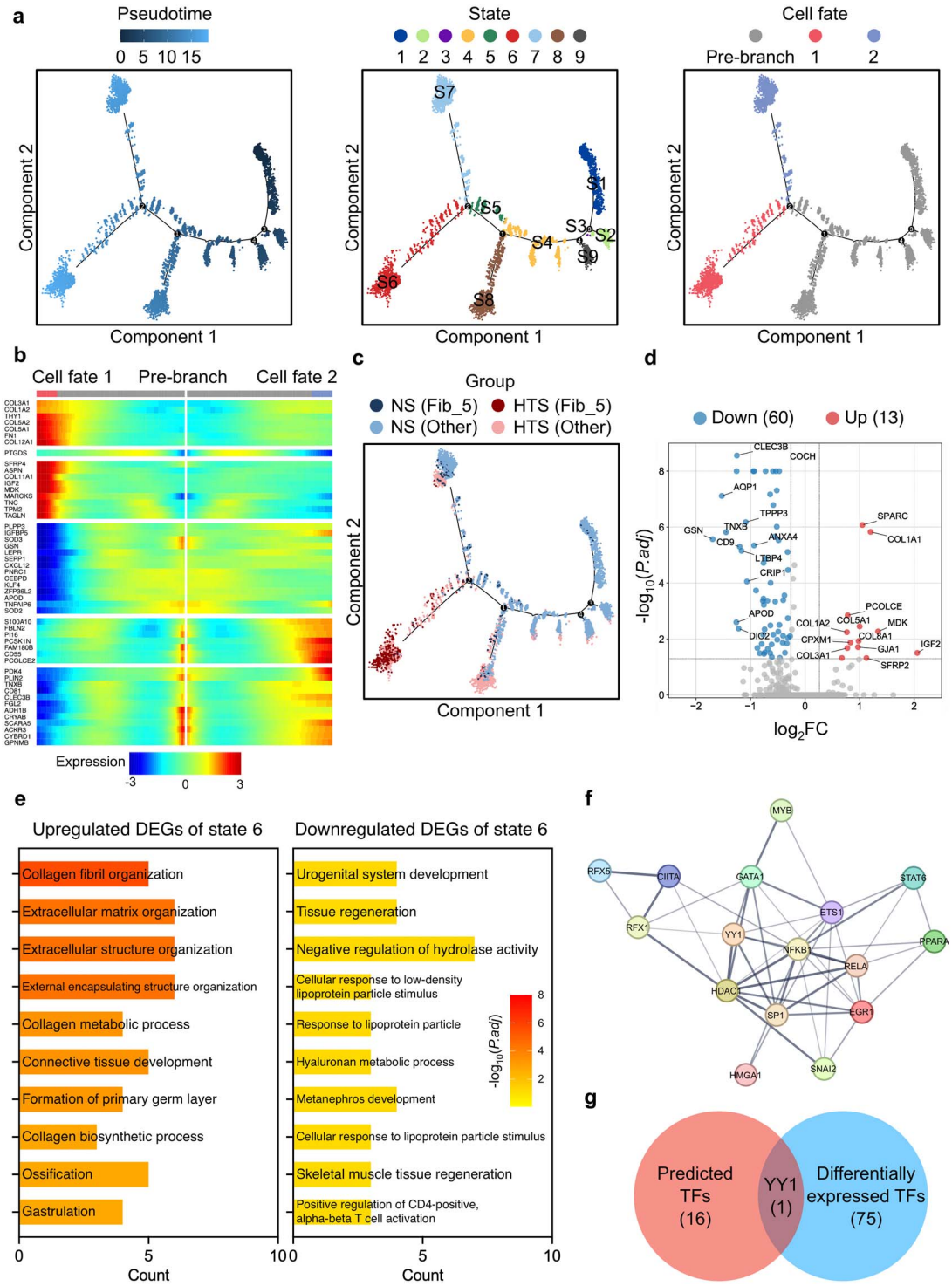


Figure 4 Transcription factor prediction from a fibroblast cell state predominant in hypertrophic scars. (**a**) Pseudotime trajectories of fibroblasts coloured by pseudotime (left), state (middle), and identified cell fates (right). (**b**) Transcriptional heatmap of Cell fate 1, Cell fate 2, and the prebranch state. (**c**) Pseudotime trajectory showing fibroblasts from different groups, with Fib_5 shown in a darker colour. (**d**) Volcano plot of DEGs in State 6 ($|\log_2 FC| > 0.25$, adjusted *P* value < 0.05). (**e**) Bar plots showing GO biological process enrichment of filtered upregulated (left) and downregulated (right) DEGs in State 6. (**f**) Protein–protein interaction network of the 16 predicted TFs. (**g**) Venn diagram of predicted TFs and differentially expressed TFs in State 6, with YY1 as the only overlapping factor. *NS* normal skin, *HTS* hypertrophic scars

Downloaded from academic.oup.com/burnstrauma/article/doi/10.1093/burnst/tkag027/8571429 by guest on 12 October 2026

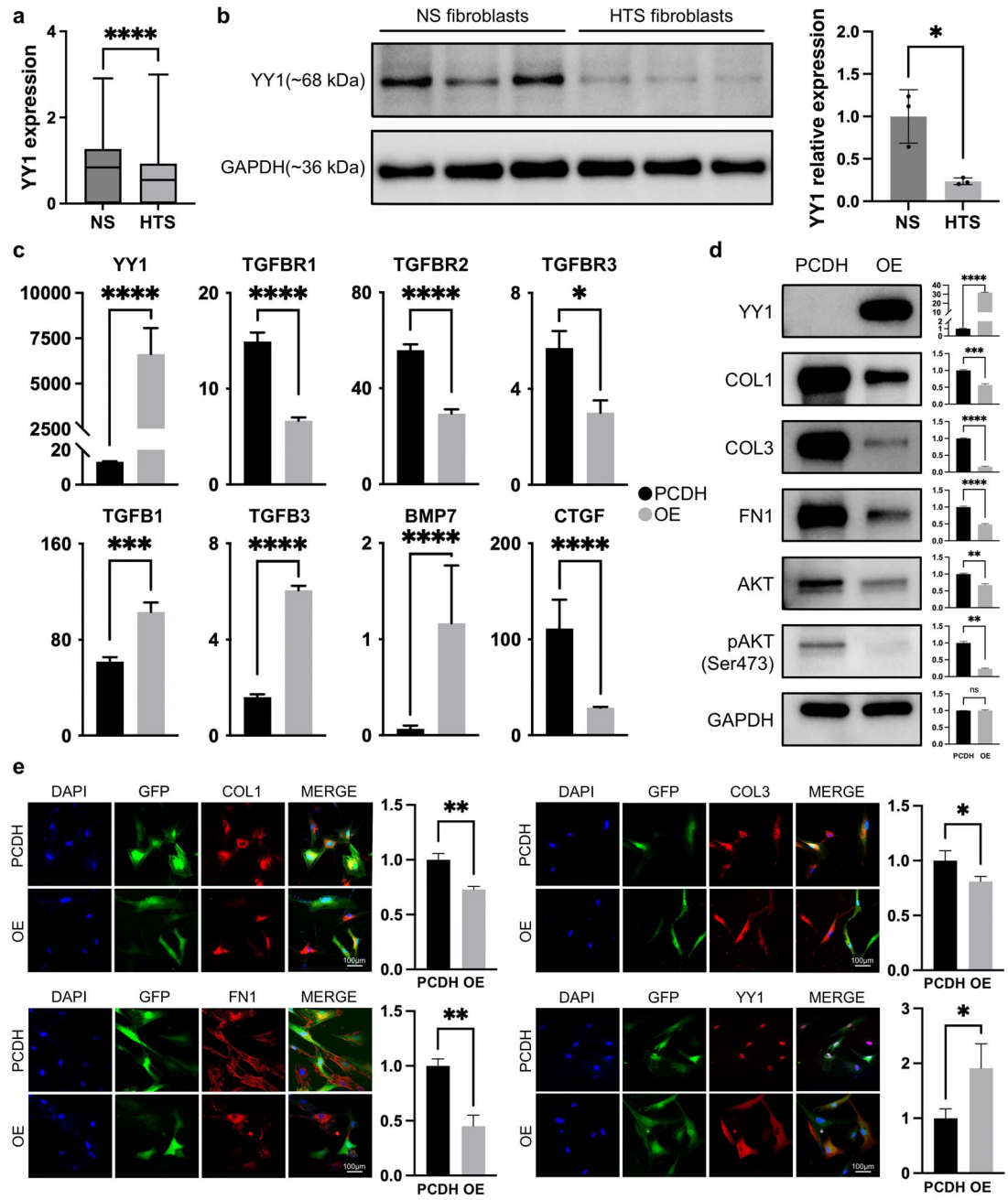


Figure 5 Overexpression of YY1 downregulates fibrosis-related gene expression. (**a**) Bar plots comparing YY1 expression between groups based on single-cell RNA sequencing data. (**b**) Western blot analysis of YY1 expression in NS and HTS fibroblasts, with three independent biological replicates per group. (**c**) Bar plots showing intergroup comparison of FPKM values for YY1 and fibrosis-related genes. (**d**) Intergroup comparison of representative western blot results from total protein extracts of control (PCDH) and YY1-overexpressing (OE) HTS fibroblasts; quantitative analyses were based on four independent biological replicates per group. (**e**) Intergroup comparison of immunofluorescence staining for FN1, COL1, COL3, and YY1. *NS* not significant, * $P < 0.05$, ** $P < 0.01$, *** $P < 0.001$, **** $P < 0.0001$. *FPKM* fragments per kilobase of exon per million mapped fragments,*GFP* green fluorescent protein, *NS* normal skin, *HTS* hypertrophic scars

($\log_2$FC = 1.73), whereas T cells showed the most pronounced decrease ($\log_2$FC = −3.53). Differential expression analysis further showed that pericytes had the largest number of upregulated DEGs, whereas fibroblasts had the largest number of downregulated DEGs. However, fibroblasts exhibited the greatest total number of DEGs, indicating the most pronounced biological differences between NS and HTS (Figure 1f).

Fibroblast subcluster 5 increased despite the overall decline in hypertrophic scar fibroblasts

Fibroblasts were subset into 13 subclusters (Fib_0–Fib_12) by unsupervised clustering to further define their heterogeneity

Downloaded from academic.oup.com/burnstrauma/article/doi/10.1093/burnst/tkag027/8571429 by guest on 12 October 2026

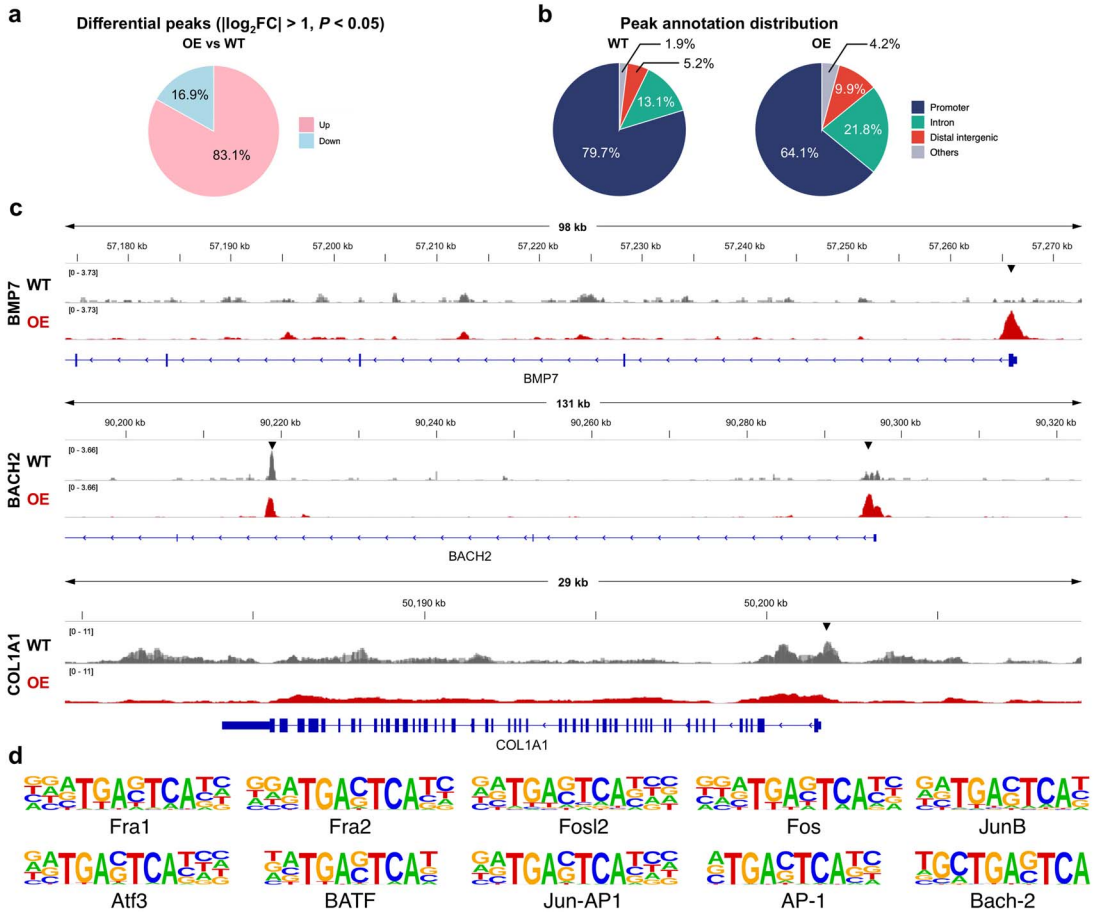


Figure 6 CUT&Tag sequencing identifies direct genomic targets of YY1 in fibroblasts. (**a**) Summary of differential peaks identified in OE *vs* WT comparison. Peaks were classified as upregulated or downregulated according to the indicated cutoff criteria ($|\log FC| > 1$, $P < 0.05$). (**b**) Genomic annotation distribution of peaks in WT and OE groups. (**c**) Specific binding peak intensities of BMP7, BACH2, and COL1A1 in WT and OE groups in IGV visualization. (**d**) The top 10 enriched motifs in peaks increased after YY1 overexpression were predominantly AP-1 family motifs, identified by HOMER *de novo* motif analysis

(Figure 2a and b). The transcriptional heatmap showed distinct transcriptomic profiles for each subcluster (Figure 2c). Intergroup compositional variability is shown in Figure 2d. As noted above, the overall fibroblast proportion was markedly reduced in HTS compared with NS; however, contrary to this decline, subcluster Fib_5 (ADAM12^{+} COMP^{+} POSTN^{hi}) showed a marked increase in HTS ($\log_2$FC = 2.52). DEGs across subclusters were analysed, filtered ($|\log_2 FC| > 0.25$, adjusted *P*-value <0.05), and totalled (Figure 2e). Fib_6 had the most upregulated DEGs, whereas Fib_5 had the most downregulated DEGs; overall, however, Fib_5 had the highest DEG count. These findings identify Fib_5 as a key subcluster with the greatest biological divergence between NS and HTS, suggesting an important role in maintaining the fibrotic phenotype of HTS. As shown in Figure 2f, this interpretation was further supported by biological process enrichment analysis of Fib_5 DEGs, which showed that the upregulated processes in this subcluster were closely linked to fibrosis, including collagen fibre and ECM organization. We then examined intergroup differences in the expression of the canonical fibrotic genes *COL1A1, COL1A2, COL3A1*, and *FN1* in Fib_5 vs other subclusters. These genes were generally upregulated in HTS fibroblasts, with Fib_5 showing the highest expression across all four genes (Figure 2g).

Cross-validation using public datasets showed that the Fib_5-like subcluster is highly conserved in hypertrophic scar

Following batch correction, several publicly available datasets were combined to generate a single-cell atlas comprising 14 NS samples and 7 HTS samples, totalling 39 609 NS dermal cells and 63 372 HTS dermal cells (Figure 3a). Cell types were annotated as described above, with the upper-right three clusters identified as fibroblasts (30 333 cells, including 11 045 NS fibroblasts and 19 288 HTS fibroblasts), and canonical marker expression is shown in Figure 3b. Fibroblasts were then subset for unsupervised clustering (Figure 3c), and public dataset fibroblast subcluster 4 (PDFS_4) showed a marked increase in the HTS group, from 2.07% to 15.35%, similar to Fib_5 (Figure 3d). Marker genes identified for Fib_5 were also upregulated in PDFS_4 (Figure 3e), prompting further examination of cluster correlation between our dataset and the public dataset. Based on either all genes or the marker genes of Fib_5, PDFS_4 and Fib_5 showed strong correlation (Figure 3f), and the cluster-to-cluster correlation matrix indicated that PDFS_4 and Fib_5 had the highest correlation (Figure 3g). Notably, despite batch correction, technical differences across

Downloaded from academic.oup.com/burnstrauma/article/doi/10.1093/burnst/tkag027/8571429 by guest on 12 October 2026

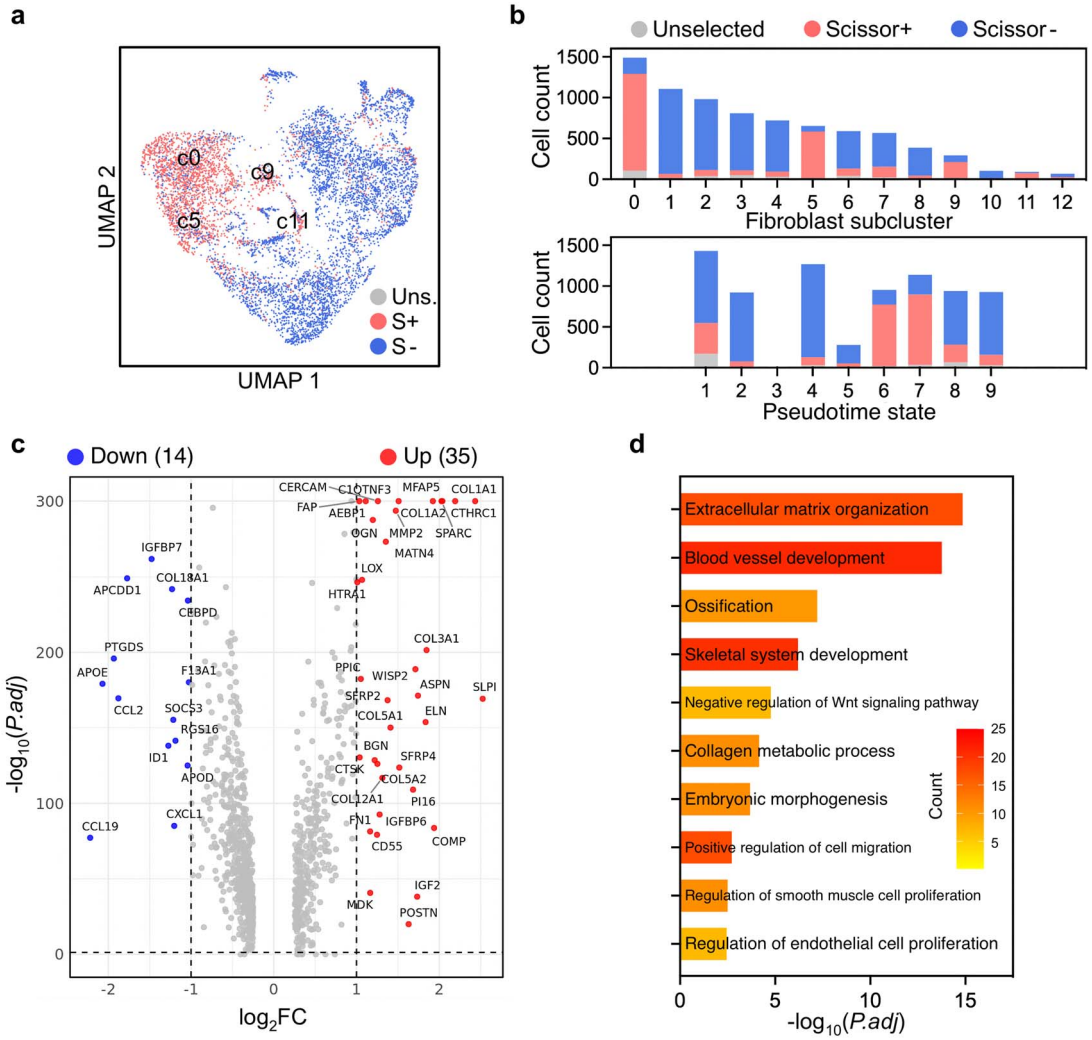


Figure 7 Scissor-positive fibroblasts responding to YY1 overexpression are crucial in hypertrophic scar formation. (**a**) UMAP visualization of the Scissor results (using an alpha of 0.05 and the binomial family). (**b**) Stacked bar plots showing the distribution of Scissor-selected cells across different subclusters (upper) and pseudotime states (lower). (**c**) Volcano plot of DEGs in Scissor-positive cells ($|\log_2 FC| > 1$, adjusted P value < 0.05). (**d**) Bar plots showing GO biological process enrichment of all filtered DEGs in Scissor-positive cells

platforms may persist and should be considered when interpreting cross-dataset comparisons.

Pseudotime analysis identified a key cell state for transcription factor prediction

Considering the intrinsic heterogeneity of dermal fibroblasts, we next performed pseudotime analysis to determine where Fib_5 was enriched along the differentiation trajectory. The fibroblast pseudotime trajectory comprised four branch points and nine cell states, of which States 6 and 7 corresponded to Cell fates 1 and 2, respectively (Figure 4a). Cells in both fates showed transcriptional features distinct from those in the pre-branch state, with collagen- and fibronectin-encoding genes markedly upregulated in Cell fate 1 (Figure 4b). Analysis of state distribution in both groups also revealed a marked increase in State 6 cells in HTS; State 6 was predominantly enriched for HTS fibroblasts, whereas NS fibroblasts predominated in State 7 (Figure 4c). The leading subclusters in State 6 were Fib_5 (48.27%), Fib_0 (18.99%), and Fib_7 (15.42%); notably, 70.34% of Fib_5 cells were distributed in State 6, 14.83% in State 7, and 5.81% in State 8. Considering the enrichment of HTS fibroblasts in State 6 and an anomalous proportional increase in Fib_5 in HTS, State 6 was appraised as a key state in HTS fibrotic pathogenesis. On examining State 6 DEGs ($|\log_2 FC| > 0.25$, adjusted P-value < 0.05), 13 upregulated and 60 downregulated DEGs were identified (Figure 4d). As shown in Figure 4e, the upregulated DEGs, including *IGF2*, *MDK*, *COL1A1*, *SFRP2*, and *SPARC*, were enriched in biological processes such as collagen fibril organization, ECM organization, extracellular structure organization, external encapsulating structure organization, and collagen biosynthetic process. Subsequently, 16 key TFs were predicted from these 73 DEGs using the TRRUST database and ranked by node degree using the Search Tool for the Retrieval of Interacting Genes/Proteins (STRING) database: HDAC1, ETS1, SP1, YY1, EGR1, NFKB1, RELA, GATA1, MYB, PPARA, STAT6, CIITA, RFX1, SNAI2, HMGA1, and RFX5 (Figure 4f). To prioritize among these predicted TFs, we further compared State 6 against the preceding state and identified differentially expressed TFs in this contrast; YY1 was the only candidate present in both analyses (Figure 4g), warranting its selection for downstream mechanistic

Downloaded from academic.oup.com/burnstrauma/article/doi/10.1093/burnst/tkag027/8571429 by guest on 12 October 2026

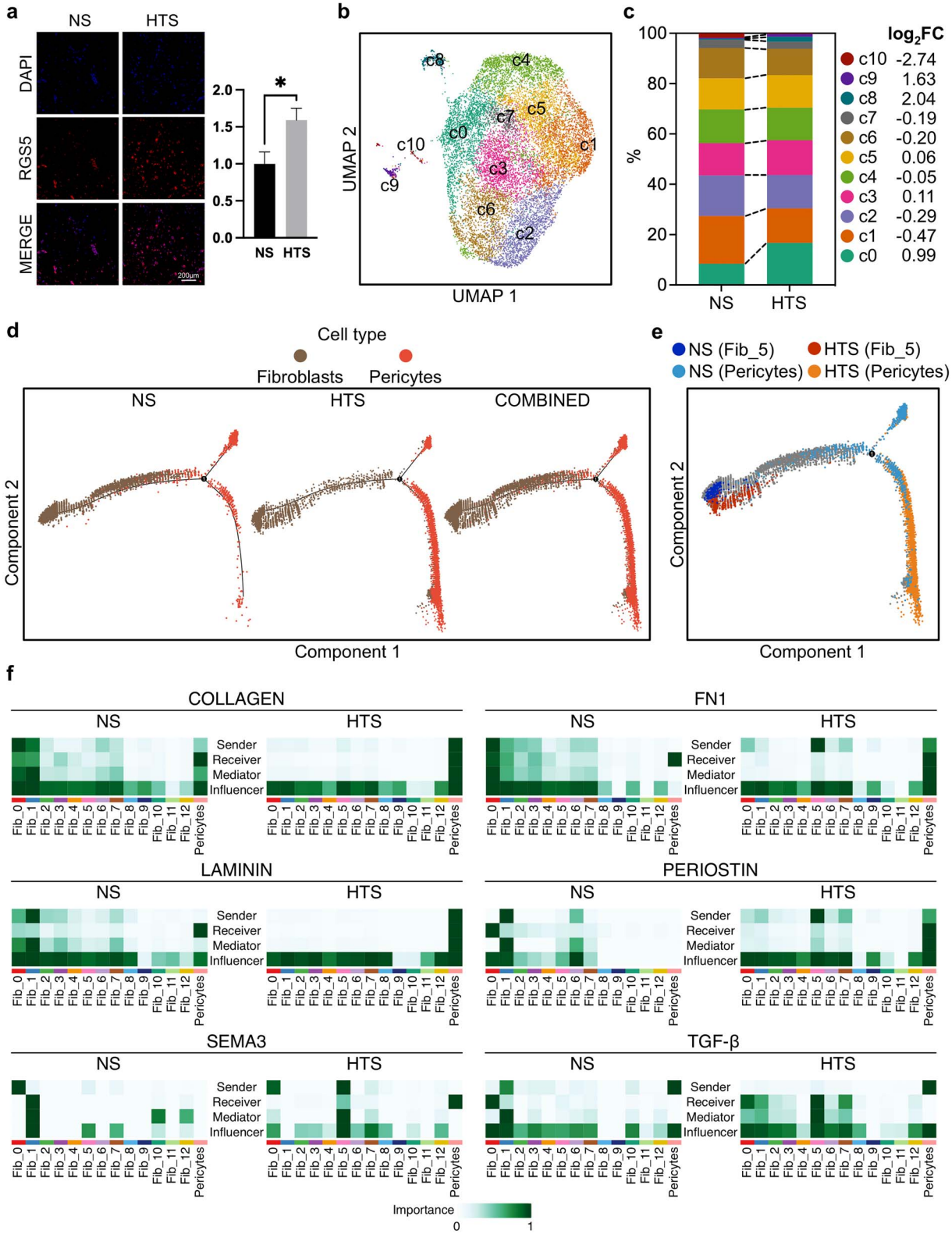


Figure 8 Homogeneous expansion of pericytes and their potential trans-differentiation relationship with fibroblasts. (**a**) Intergroup comparison of RGS5 immunofluorescence staining. (**b**) UMAP visualization of pericytes reclustered into 11 subclusters by unsupervised clustering. (**c**) Stacked percentage plot showing differences in the proportions of pericyte subclusters between NS and HTS. (**d**) Pseudotime trajectories from joint analysis of fibroblasts and pericytes, coloured by cell type (left). (**e**) Pseudotime trajectory of the merged dataset, coloured by group and cell type, suggesting a potential *trans*-differentiation relationship between pericytes and Fib_5. (**f**) Centrality score heatmaps of selected significant signalling pathways identified by CellChat. * $P < 0.05$. *UMAP* Uniform Manifold Approximation and Projection, *NS* normal skin, *HTS* hypertrophic scars

Downloaded from academic.oup.com/burnstrauma/article/doi/10.1093/burnst/tkag027/8571429 by guest on 12 October 2026

investigation. Previous studies have identified significant associations between YY1 and fibrosis in the heart, kidney, and lung, yet no study to date has examined its role in the skin.

Overexpression of YY1 downregulated fibrotic gene expression in hypertrophic scar fibroblasts

To investigate the role of YY1 in HS fibrotic pathogenesis, we first examined YY1 expression in fibroblasts from NS and HTS at both the messenger RNA (mRNA) and protein levels. As shown in the box plot (Figure 5a), YY1 expression was downregulated in the HTS group at the mRNA level. In addition, western blotting of total protein extracts from fibroblasts in both groups showed significantly reduced YY1 protein expression in HTS fibroblasts (Figure 5b). We then constructed YY1-overexpressing plasmid vectors to determine whether YY1 could modulate the expression of fibrosis-associated genes in HTS fibroblasts. The YY1 gene sequence was first aligned with the multiple cloning site of the pCDH-CMV-MCS-EF1-CopGFP plasmid vector, and XbaI (T^CTAGA) and NheI (G^CTAGC) were selected as restriction sites. After ligation, the YY1-pCDH overexpression plasmid was quality-checked by digestion and gel electrophoresis. Lentiviruses produced by HEK 293 T cells were used to infect HTS fibroblasts, and successful overexpression was confirmed by transcriptomic RNA-sequencing. As illustrated in Figure 5c, bulk-seq results showed significantly increased YY1 expression in the overexpression group (OE) compared with that of the control group (PCDH); although the expression of the profibrotic transforming growth factor beta-1 (TGFB1) remained upregulated in the OE group, other canonical genes involved in organ fibrosis showed changes indicative of a transition towards an antifibrotic phenotype. Additionally, western blot results showed a significant increase in YY1 and marked reductions in COL1, COL3, FN1, AKT, and p-AKT in the OE group at the protein level (Figure 5d). These findings were further supported by the increased immunofluorescence staining of YY1, together with marked reductions in COL1, COL3, and FN1 in YY1-overexpressing HTS fibroblasts (Figure 5e).

To further define the direct downstream targets of YY1, we performed YY1 CUT&Tag sequencing in BJ human fibroblasts with YY1 knockdown (KD), YY1 overexpression (OE), or no treatment (WT), using three biological replicates per group. De novo motif analysis confirmed the specificity of the assay, with YY1 identified as the most enriched motif in peaks diminished upon knockdown ($P = 1 \times 10^{-48}$; Supplementary Dataset 1). Differential peak analysis ($|\log FC| > 1$, $P < .05$) showed that OE predominantly increased YY1 binding, with 83% of the 15 857 differential peaks exhibiting enhanced occupancy (Figure 6a). Peak annotation analysis revealed that YY1-binding sites were mainly enriched in promoter regions, consistent with its established role as a promoter-binding TF. Under OE conditions, however, the proportion of promoter-associated peaks decreased, whereas the proportions of intronic and distal intergenic peaks increased, suggesting that YY1 overexpression not only reinforced promoter binding but also expanded occupancy to other regulatory elements (Figure 6b). Differentially bound genes included several fibrosis-related targets. In particular, YY1 binding at antifibrotic genes BMP7 (log2FC = 3.52, $P = 0.0004$) and BACH2 (log2FC = 1.84, $P = 0.0005$) was significantly increased upon overexpression, whereas binding at the profibrotic gene COL1A1 was significantly reduced (log2FC = −0.39, $P = 0.022$) (Figure 6c; Supplementary Dataset 2). Notably, HOMER *de novo* motif analysis revealed that 9 of the top 10 enriched motifs in peaks gained upon YY1 overexpression belonged to the AP-1 family (Figure 6d, Supplementary Dataset 1). This suggests that YY1 may exert antifibrotic effects, at least in part, by occupying AP-1-associated regulatory elements and antagonizing AP-1-driven fibrogenic transcription.

Subsequently, we used the Scissor package to jointly analyse the scRNA-seq and bulk-seq data to identify the fibroblast populations that responded to YY1 overexpression. The Scissor results, generated using an alpha of 0.05 and a binomial family, were visualized using UMAP (Figure 7a), with the positive region primarily overlapping Fib_0, Fib_5, and Fib_9. Specifically, most Scissor-positive cells belonged to Fib_0 (46.66%) and Fib_5 (22.33%) or to State 6 (29.52%) and State 7 (33.92%) based on the states identified by pseudotime analysis (Figure 7b). The DEGs ($|\log_2 FC| > 1$, adjusted P-value < 0.05) of Scissor-positive cells, compared with those of other cells, comprised 35 upregulated and 14 downregulated genes (Figure 7c), which were enriched in key biological processes involved in HTS formation, such as ECM organization and blood vessel development (Figure 7d).

Homogeneously expanded pericytes may be linked to the key fibroblast subcluster in hypertrophic scar

As shown above, pericytes also underwent marked expansion in HTS, which was further supported by increased immunofluorescence staining of RGS5 (Figure 8a), a marker of activated pericytes in HTS. To determine whether pericytes showed a disproportionate pattern of subcluster expansion similar to that of fibroblasts, unsupervised clustering was performed separately on the pericyte subsets. As shown in Figure 8b and c, pericyte expansion between groups was relatively uniform across subclusters.

As previous studies have shown that pericytes contribute to fibroblast populations in tissue fibrosis [37–43], we next performed joint pseudotime analysis on the merged pericyte and fibroblast dataset (Figure 8d). As shown in Figure 8e, pseudotime analysis delineated a bifurcating trajectory comprising three states, with pericytes positioned at the start of the trajectory and Fib_5 at the terminal fibrotic state. This suggests a potential differentiation trajectory from pericytes towards the Fib_5 fibrotic phenotype in HTS. We then focused on fibroblast–pericyte communication dynamics to explore potential intergroup functional reprogramming. As shown in Figure 8f, centrality scores of fibrosis-associated signalling pathways revealed marked alterations, with pericytes alone or together with Fib_5 acting as principal effectors in HTS. Notably, these centrality scores represent relative importance normalized within each condition; therefore, statistical comparisons between conditions were not applicable.

Discussion

Hypertrophic scars impose a substantial clinical burden, often causing pain, pruritus, and restricted movement, underscoring the need for more effective targeted therapies. In this study, we performed scRNA-seq on the dermis to generate a dermal cell atlas

Downloaded from academic.oup.com/burnstrauma/article/doi/10.1093/burnst/tkag027/8571429 by guest on 12 October 2026

specific to HTS pathogenesis. Fibroblasts, particularly myofibroblasts, have long been implicated in HTS pathogenesis, but their characterization remains challenging because of their inherent heterogeneity. The diverse functional states of fibroblasts, ranging from matrix-secreting to pro-inflammatory subtypes, complicate therapeutic targeting. Solé-Boldo *et al.* [24] suggested that fibroblasts can be further divided into four subtypes, namely, secretory-reticular, secretory-papillary, pro-inflammatory, and mesenchymal fibroblasts; in this study, Fib_5 corresponded to the mesenchymal subtype. Deng *et al.* [12] confirmed that mesenchymal fibroblasts associated with collagen overexpression are significantly increased in fibrotic skin diseases, consistent with our observation that Fib_5 expanded despite the overall decline in HTS fibroblasts. Li *et al.* [44] identified five disease-specific fibroblast populations, namely, PLCG2_Fibroblast, P311_Fibroblast, GPX3_Fibroblast, APCDD1_Fibroblast, and other fibroblasts across four fibrotic skin states, including NS, scar, keloid, and scleroderma, and identified IRF4 as a fate-determining regulator of scar-associated GPX3_Fibroblast. Hong *et al.* [9] showed that a fibroblast subcluster with elevated TEM1 (CD248) expression is crucial in pathologic scarring; herein, Fib_5 also showed the highest mean expression of TEM1 among all fibroblast subclusters. Considering the relatively small sample size of our dataset, we downloaded publicly available sequencing data from five additional studies, integrated the datasets, and repeated the same analyses. We found that a subcluster highly correlated with Fib_5 also increased markedly in the HTS group of the public dataset, indicating that this fibrosis-related subcluster is highly conserved in HTS.

TFs are indispensable for maintaining homeostasis, and their dysregulation is observed in various diseases [45]. Targeting TFs represents a promising yet largely unexplored therapeutic avenue for HTS. Doeser *et al.* [46] reported that transient induction of certain TFs in murine cutaneous wounds downregulated fibrotic gene expression and thereby reduced scar formation. Wang *et al.* [47] identified that suppressed transcription of peroxisome proliferator–activated receptors contributes to hypertrophic scar formation. Our previous study [14] also found that fetuin-A could mitigate the fibrotic properties of HTS fibroblasts by upregulating the TF ETV4. In the present study, we identified 75 TFs that were significantly differentially expressed between State 6 and its preceding state; among these, only YY1 overlapped with the 16 TFs predicted in State 6. YY1 is a multifunctional zinc finger TF that is instrumental in cell proliferation, differentiation, and apoptosis [48–50]. Its role in fibrosis varies across organs. Jin *et al.* [51] identified YY1 as a key TF in keloid fibroblasts that promotes keloid pathogenesis by enhancing oxidative stress and inflammation. Yang *et al.* [52] reported that reduced YY1 reversed epithelial–mesenchymal transition and ameliorated consequent renal fibrosis. Meanwhile, Chen *et al.* [53] demonstrated that YY1 knockout exerted protective effects against pulmonary fibrosis. Conversely, Tan *et al.* [54] and Huang *et al.* [55] showed that YY1 protects against cardiac fibrosis. Despite its context-dependent pro- or anti-fibrotic roles in different tissues, YY1 was found to be downregulated in HTS fibroblasts.

Accordingly, we hypothesized that restoring YY1 expression would repress fibrosis-related gene expression, and indeed, YY1 overexpression significantly reduced the expression of key fibrosis-associated genes, including *FN1*, *COL1A1*, and *COL3A1*. Therefore, restoring YY1 expression in HTS fibroblasts may attenuate fibrotic programmes and partly reverse the fibrotic phenotype, supporting YY1 as a potential therapeutic target in HTS. To further elucidate the antifibrotic mechanism of YY1 in HTS fibroblasts, we examined changes in genes previously implicated in fibrosis. Despite upregulation of the profibrotic TGFB1 in YY1-overexpressing fibroblasts, expression of its receptors was downregulated, whereas the antifibrotic transforming growth factor beta-3 was upregulated. Tan *et al.* [54] found that YY1 could upregulate bone morphogenetic protein 7 and downregulate connective tissue growth factor to suppress cardiac fibrosis, which was also observed in YY1-overexpressing fibroblasts. Taken together, YY1 may exert antifibrotic effects by downregulating receptors of the canonical TGF-β pathway, thereby attenuating downstream fibrogenic signalling. Additionally, AKT and its activated form, phosphorylated AKT (p-AKT), have been reported to play important roles in organ fibrosis [56–60] and contribute to HTS development and persistence [61]. Consistent with previous studies [62–67], YY1 overexpression also downregulated AKT and p-AKT expression, as confirmed by western blotting. Thus, YY1 exerts its antifibrotic effects in HTS fibroblasts through multiple mechanisms, including modulation of TGF-β and AKT signalling pathways, which should be validated in future *in vivo* studies.

Additionally, our CUT&Tag analysis validated these findings at the epigenomic level, demonstrating that YY1 directly binds to the regulatory regions of fibrosis-related genes. Strikingly, motif analysis revealed extensive co-occupancy of YY1 and AP-1 motifs at shared regulatory elements. AP-1 family (comprising Jun and Fos subunits) is a versatile dimeric TF family that has been demonstrated to play a crucial role in advancing tissue and organ fibrosis via induction of the expression of fibrotic molecules and activating fibroblasts [68]. Our findings suggest that YY1 may counteract AP-1-driven fibrogenic transcription, a mechanism previously unrecognized in skin fibrosis that warrants further investigation.

Lastly, pericytes showed markedly increased abundance in HTS dermis, consistent with the pathological angiogenesis characteristic of scar progression. Beyond angiogenesis, pericytes may also contribute to the fibrotic phenotype. Using lineage tracing, Dulauroy *et al.* [69] showed that pericytes are a major source of dermal myofibroblasts in scars; pericytes have also been reported to contribute to fibroblast populations in multiple fibrotic organs [37–43]. In this context, our pseudotime analysis suggested that pericytes may support the fibrotic phenotype of HTS by transdifferentiating into mesenchymal fibroblasts, although this requires further validation. Nevertheless, intercellular communication analysis further highlighted marked reprogramming of fibroblast–pericyte signalling across multiple fibrosis-associated pathways in HTS. In the collagen and laminin pathways, pericytes replaced fibroblasts as the primary sender in HTS, indicating greater importance in ECM synthesis under fibrotic conditions. In the FN1, POSTN, and SEMA3 pathways, Fib_5 emerged as the predominant sender and pericytes as the principal receiver, underscoring novel profibrotic crosstalk between these populations. Despite variation in the marker genes of fibrotic subclusters identified across studies, a consistent feature is upregulated periostin expression, which has been reported to promote fibroblast proliferation and persistence of myofibroblasts in HTS [70]. Recent studies demonstrated that POSTN significantly promotes pericyte proliferation, thereby facilitating collagen production and scar formation after spinal cord injury [71]. In addition, the SEMA3 signalling pathway, which has been reported to drive

Downloaded from academic.oup.com/burnstrauma/article/doi/10.1093/burnst/tkag027/8571429 by guest on 12 October 2026

myofibroblast differentiation and activation [72, 73], is critical for vascular integrity. Finally, in the TGF-β pathway, the primary receiver shifted from Fib_0 in NS to Fib_5 in HTS, highlighting Fib_5 as a critical responder in canonical fibrogenic signalling. Thus, Fib_5 may drive pericytes towards an activated profibrotic state, positioning these cells as key collaborators in sustaining the fibrotic phenotype in HTS and offering new insight into cellular interactions in HTS.

Conclusions

This study identifies a conserved mesenchymal fibroblast cluster Fib_5 (ADAM12^{+} COMP^{+} POSTN^{hi}) in HTS and shows that restoring YY1 expression may reprogramme HTS fibroblasts away from the fibrotic state, highlighting the Fib_5-YY1 axis as a core transcriptional module underlying fibroblast plasticity in HTS.

List of abbreviations

BEAM, branched expression analysis modelling; CCA, canonical correlation analysis; DEG, differentially expressed gene; ECM, extracellular matrix; FPKM, fragments per kilobase of exon per million mapped fragments; GEO, gene expression omnibus; GO, Gene Ontology; HTS, hypertrophic scar; HVG, highly variable gene; KEGG, Kyoto Encyclopedia of Genes and Genomes; OE, overexpression; PCDH, pCDH empty-vector control; scRNA-seq, single-cell RNA sequencing; STRING, Search Tool for the Retrieval of Interacting Genes/Proteins; TF, transcription factor; UMAP, Uniform Manifold Approximation and Projection.

Acknowledgements

Not applicable.

Author contributions

Qian Yu (Data curation, Formal analysis, Investigation, Methodology, Validation [lead], Software, Visualization, Writing—original draft [equal]), Zonglin Huang (Data curation, Formal analysis, Software, Validation, Visualization, Writing—original draft [equal]), Lei Cai (Project administration, Resources, Supervision, Writing—review & editing [equal]), Yanze Lv (Writing—review & editing [supporting]), Lianzhao Wang (Data curation [supporting]), Huanhuan Wu (Data curation [supporting]), Qiang Dai (Methodology, Validation [supporting]), Zikai Qiu (Methodology, Validation [equal]), Zhigang Yang (Project administration, Resources, Supervision), Xin Fu (Methodology, Project administration, Supervision, Writing—review & editing [equal]), Ran Xiao (Conceptualization, Project administration, Resources, Supervision [lead])

Supplementary material

Supplementary material is available at *Burns & Trauma* online.

Ethics approval and consent to participate

The study was approved by the Ethics Committee of the Plastic Surgery Hospital, Chinese Academy of Medical Sciences (2021(179)). Written consent was obtained from all patients prior to the surgeries using a consent form.

Conflicts of interest

None declared.

Funding

National Natural Science Foundation of China (32370884, 82073468) and Chinese Academy of Medical Sciences Initiative for Innovative Medicine (CAMS-I2M) (2021-I2M-1-052).

Data availability

The raw sequence data generated in the current study have been deposited in the Genome Sequence Archive in National Genomics Data Center, China National Center for Bioinformation/Beijing Institute of Genomics, Chinese Academy of Sciences (accession number: HRA011392) that are publicly accessible at https://ngdc.cncb.ac.cn/gsa-human. The data that support the findings of this study are available in the NCBI GEO repository, https://www.ncbi.nlm.nih.gov/geo/, with accession numbers of GSE130973, GSE151177, GSE156326, GSE181316, and GSE243716.

References

1. Liu M, Liu X, Zhang J, Liang S, Gong Y, Shi S, *et al.* Single-cell RNA sequencing reveals the heterogeneity of myofibroblasts in wound repair. *Genomics* 2025;117:110982. https://doi.org/10.1016/j.ygeno.2024.110982.
2. Xie S, Huang R, Qian W, Ding X, Zhang W, Li Y, *et al.* Globotriaosylceramide Gb3 influences wound healing and scar formation by orchestrating fibroblast heterogeneity. *Adv Sci Weinh Baden-Wurtt Ger* 2025;12:e09733. https://doi.org/10.1002/advs.202509733.
3. Yao H, Jing SL, Huang KX, Griffin MF, Longaker MT, Wan DC, *et al.* Clinical features and mechanisms of differential wound healing and scarring across anatomical sites. *Adv Wound Care* published online 10 Nov 2025. https://doi.org/10.1177/21621918251387627.
4. Griffin M, Guo JL, Parker JBL, Kuhnert M, Li DJ, Valencia C, *et al.* Multi-omic analysis reveals retinoic acid molecular drivers for dermal fibrosis and regenerative repair in the skin. *Cell Stem Cell* 2025;32:1421–1437.e6. https://doi.org/10.1016/j.stem.2025.07.010.
5. Cheng X, Gao Z, Shan S, Shen H, Zheng H, Jin L, *et al.* Single cell transcriptomics reveals the cellular heterogeneity of keloids and the mechanism of their aggressiveness. *Commun Biol* 2024;7:1–12. https://doi.org/10.1038/s42003-024-07311-1.
6. Bodnar RJ, Satish L, Yates CC, Wells A. Pericytes: a newly recognized player in wound healing. *Wound Repair Regen* 2016;24:204–14. https://doi.org/10.1111/wrr.12415.
7. Liu X, Chen W, Zeng Q, Ma B, Li Z, Meng T, *et al.* Single-cell RNA-sequencing reveals lineage-specific regulatory changes of fibroblasts and vascular endothelial cells in keloids. *J Invest Dermatol* 2022;142:124–135.e11. https://doi.org/10.1016/j.jid.2021.06.010.

Downloaded from academic.oup.com/burnstrauma/article/doi/10.1093/burnst/tkag027/8571429 by guest on 12 October 2026

8. Wang Y, Zhou X, Liu M, Huang M, Chen P, Li X, *et al.* Targeting NRP1 in endothelial cells facilitates the normalization of scar vessels and prevents fibrotic scarring. *Adv Sci Weinh Baden-Wurtt Ger* 2025;13:e10545. https://doi.org/10.1002/advs.202510545.
9. Hong YK, Lin YC, Cheng TL, Lai CH, Chang YH, Huang YL, *et al.* TEM1/endosialin/CD248 promotes pathologic scarring and TGF-β activity through its receptor stability in dermal fibroblasts. *J Biomed Sci* 2024;31:12. https://doi.org/10.1186/s12929-024-01001-0.
10. Zhang S, Zhang Y, Min P. Single-cell and bulk transcriptome data integration reveals dysfunctional cell types and aberrantly expressed genes in hypertrophic scar. *Front Genet* 2021;12:806740. https://doi.org/10.3389/fgene.2021.806740.
11. Zhao S, Xie J, Zhang Q, Ni T, Lin J, Gao W, *et al.* New antifibrotic strategies for keloids: insights from single-cell multi-Omics. *Cell Prolif* 2025;58:e13818. https://doi.org/10.1111/cpr.13818.
12. Deng W, Ma Y, Su Z, Liu Y, Liang P, Huang C. *et al.* Single-cell RNA-sequencing analyses identify heterogeneity of CD8+ T cell subpopulations and novel therapy targets in melanoma. *Mol Ther Oncolytics* 2021;20:105–18. https://doi.org/10.1016/j.omto.2020.12.003.
13. Han C, Yuan H, Koh TJ, Chen L, Mecham RP, DiPietro LA. Loss of MFAP5 and its effect on skin homeostasis and wound healing. *FASEB J* 2025;39:e71273. https://doi.org/10.1096/fj.202501770R.
14. Yu Q, Dai Q, Huang Z, Li C, Yan L, Fu X, *et al.* Microfat exerts an anti-fibrotic effect on human hypertrophic scar via fetuin-A/ETV4 axis. *J Transl Med* 2023;21:231. https://doi.org/10.1186/s12967-023-04065-y.
15. Zhong XC, Chen CY, Feng ZX, Wang Y, Zhang T, Zhuang ZM, *et al.* Hsa_circ_0026782 acts as a 'molecular break' of CREB1-mediated transcription by promoting its phosphorylation at Ser142 that prevents keloid progression. *Adv Sci Weinh Baden-Wurtt Ger* 2025;12:e08647. https://doi.org/10.1002/advs.202508647.
16. McGinnis CS, Murrow LM, Gartner ZJ. DoubletFinder: doublet detection in single-cell RNA sequencing data using artificial nearest neighbors. *Cell Syst* 2019;8:329–337.e4. https://doi.org/10.1016/j.cels.2019.03.003.
17. Stuart T, Butler A, Hoffman P, Hafemeister C, Papalexi E, Mauck WM III, *et al.* Comprehensive integration of single-cell data. *Cell* 2019;177:1888–1902.e21. https://doi.org/10.1016/j.cell.2019.05.031.
18. Yu G, Wang LG, Han Y, He QY. clusterProfiler: an R package for comparing biological themes among gene clusters. *OMICS J Integr Biol* 2012;16:284–7. https://doi.org/10.1089/omi.2011.0118.
19. Zhou Y, Zhou B, Pache L, Chang M, Khodabakhshi AH, Tanaseichuk O, *et al.* Metascape provides a biologist-oriented resource for the analysis of systems-level datasets. *Nat Commun* 2019;10:1523. https://doi.org/10.1038/s41467-019-09234-6.
20. Cao J, Spielmann M, Qiu X, Huang X, Ibrahim DM, Hill AJ, *et al.* The single-cell transcriptional landscape of mammalian organogenesis. *Nature* 2019;566:496–502. https://doi.org/10.1038/s41586-019-0969-x.
21. Han H, Cho JW, Lee S, Yun A, Kim H, Bae D, *et al.* TRRUST v2: an expanded reference database of human and mouse transcriptional regulatory interactions. *Nucleic Acids Res* 2018;46:D380–6. https://doi.org/10.1093/nar/gkx1013.
22. Sun D, Guan X, Moran AE, Wu LY, Qian DZ, Schedin P, *et al.* Identifying phenotype-associated subpopulations by integrating bulk and single-cell sequencing data. *Nat Biotechnol* 2022;40:527–38. https://doi.org/10.1038/s41587-021-01091-3.
23. Jin S, Plikus MV, Nie Q. CellChat for systematic analysis of cell–cell communication from single-cell transcriptomics. *Nat Protoc* 2025;20:180–219. https://doi.org/10.1038/s41596-024-01045-4.
24. Solé-Boldo L, Raddatz G, Schütz S, Mallm JP, Rippe K, Lonsdorf AS, *et al.* Single-cell transcriptomes of the human skin reveal age-related loss of fibroblast priming. *Commun Biol* 2020;3:188. https://doi.org/10.1038/s42003-020-0922-4.
25. Kim J, Lee J, Kim HJ, Kameyama N, Nazarian R, der E, *et al.* Single-cell transcriptomics applied to emigrating cells from psoriasis elucidate pathogenic versus regulatory immune cell subsets. *J Allergy Clin Immunol* 2021;148:1281–92. https://doi.org/10.1016/j.jaci.2021.04.021.
26. Vorstandlechner V, Laggner M, Copic D, Klas K, Direder M, Chen Y, *et al.* The serine proteases dipeptidyl-peptidase 4 and urokinase are key molecules in human and mouse scar formation. *Nat Commun* 2021;12:6242. https://doi.org/10.1038/s41467-021-26495-2.
27. Direder M, Weiss T, Copic D, Vorstandlechner V, Laggner M, Pfisterer K, *et al.* Schwann cells contribute to keloid formation. *Matrix Biol J Int Soc Matrix Biol* 2022;108:55–76. https://doi.org/10.1016/j.matbio.2022.03.001.
28. Love MI, Huber W, Anders S. Moderated estimation of fold change and dispersion for RNA-seq data with DESeq2. *Genome Biol* 2014;15:550. https://doi.org/10.1186/s13059-014-0550-8.
29. Chen Y, Lun ATL, Smyth GK. From reads to genes to pathways: differential expression analysis of RNA-Seq experiments using Rsubread and the edgeR quasi-likelihood pipeline. *F1000Res* 2016;5:1438.
30. Kaya-Okur HS, Wu SJ, Codomo CA, Pledger ES, Bryson TD, Henikoff JG, *et al.* CUT&tag for efficient epigenomic profiling of small samples and single cells. *Nat Commun* 2019;10:1930. https://doi.org/10.1038/s41467-019-09982-5.
31. Chen S, Zhou Y, Chen Y, Gu J. Fastp: an ultra-fast all-in-one FASTQ preprocessor. *Bioinf (Oxf)* 2018;34:i884–90. https://doi.org/10.1093/bioinformatics/bty560.
32. Md V, Misra S, Li H, Aluru S. Efficient Architecture-Aware Acceleration of BWA-MEM for Multicore Systems. In *2019 IEEE Int Parallel Distrib Process Symp* (IPDPS), Brazil, Rio de Janeiro, 2019, 314–24.
33. Zhang Y, Liu T, Meyer CA, Eeckhoute J, Johnson DS, Bernstein BE, *et al.* Model-based analysis of ChIP-Seq (MACS). *Genome Biol* 2008;9:R137. https://doi.org/10.1186/gb-2008-9-9-r137.
34. Heinz S, Benner C, Spann N, Bertolino E, Lin YC, Laslo P, *et al.* Simple combinations of lineage-determining transcription factors prime cis-regulatory elements required for macrophage and B cell identities. *Mol Cell* 2010;38:576–89. https://doi.org/10.1016/j.molcel.2010.05.004.
35. Yu G, Wang LG, He QY. ChIPseeker: an R/Bioconductor package for ChIP peak annotation, comparison and visualization. *Bioinf (Oxf)* 2015;31:2382–3. https://doi.org/10.1093/bioinformatics/btv145.

Downloaded from academic.oup.com/burnstrauma/article/doi/10.1093/burnst/tkag027/8571429 by guest on 12 October 2026

36. Quinlan AR, Hall IM. BEDTools: a flexible suite of utilities for comparing genomic features. *Bioinf (Oxf)* 2010;26:841–2. https://doi.org/10.1093/bioinformatics/btq033.
37. Tuleta I, Frangogiannis NG. Pericytes in tissue fibrosis. *Am J Physiol Cell Physiol* 2025;329:C868–86. https://doi.org/10.1152/ajpcell.00403.2025.
38. van Splunder H, Villacampa P, Martínez-Romero A, Graupera M. Pericytes in the disease spotlight. *Trends Cell Biol* 2024;34:58–71. https://doi.org/10.1016/j.tcb.2023.06.001.
39. L Alex, I Tuleta, SC Hernandez, A Hanna, H Venugopal, M Astorkia, *et al*. Cardiac Pericytes Acquire a Fibrogenic Phenotype and Contribute to Vascular Maturation After Myocardial Infarction. *Circulation* 2023;**148**:882–98. https://doi.org/10.1161/CIRCULATIONAHA.123.064155.
40. Zhao Z, Zhang Y, Zhang C, Zhang J, Luo X, Qiu Q, *et al.* TGF-β promotes pericyte-myofibroblast transition in subretinal fibrosis through the Smad2/3 and Akt/mTOR pathways. *Exp Mol Med* 2022;54:673–84. https://doi.org/10.1038/s12276-022-00778-0.
41. Hosaka K, Yang Y, Seki T, Fischer C, Dubey O, Fredlund E, *et al.* Pericyte–fibroblast transition promotes tumor growth and metastasis. *Proc Natl Acad Sci* 2016;113:E5618–27. world. https://doi.org/10.1073/pnas.1608384113.
42. Lin SL, Kisseleva T, Brenner DA, Duffield JS. Pericytes and perivascular fibroblasts are the primary source of collagen-producing cells in obstructive fibrosis of the kidney. *Am J Pathol* 2008;173:1617–27. https://doi.org/10.2353/ajpath.2008.080433.
43. Humphreys BD, Lin SL, Kobayashi A, Hudson TE, Nowlin BT, Bonventre JV, *et al.* Fate tracing reveals the pericyte and not epithelial origin of myofibroblasts in kidney fibrosis. *Am J Pathol* 2010;176:85–97. https://doi.org/10.2353/ajpath.2010.090517.
44. Li Y, Li C, Liu W, Gao T, Liu Q, Yang L, *et al.* Single-cell RNA sequencing reveals fibroblast heterogeneity and identifies CLOCK as a key regulator in fibrotic skin diseases. *Sci Rep* 2025;16:786. https://doi.org/10.1038/s41598-025-30260-6.
45. Lambert SA, Jolma A, Campitelli LF, das PK, Yin Y, Albu M, *et al.* The human transcription factors. *Cell* 2018;175:598–9. https://doi.org/10.1016/j.cell.2018.09.045.
46. Doeser MC, Schöler HR, Wu G. Reduction of fibrosis and scar formation by partial reprogramming In vivo. *Stem Cells* 2018;36:1216–25. https://doi.org/10.1002/stem.2842.
47. Wang J, Du J, Song Y, Tan X, Wu J, Wang T, *et al.* CILP1 interacting with YBX1 promotes hypertrophic scar formation by suppressing PPARs transcription. *Cell Death Dis* 2025;16:371. https://doi.org/10.1038/s41419-025-07554-8.
48. Martins Peçanha FL, Jaafar R, Werneck-de-Castro JP, Apostolopolou CC, Bhushan A, Bernal-Mizrachi E. The transcription factor YY1 is essential for Normal DNA repair and cell cycle in human and mouse β-cells. *Diabetes* 2022;71:1694–705. https://doi.org/10.2337/db21-0908.
49. Ou X, Huo J, Huang Y, Li YF, Xu S, Lam KP. Transcription factor YY1 is essential for iNKT cell development. *Cell Mol Immunol* 2019;16:547–56. https://doi.org/10.1038/s41423-018-0002-6.
50. Weintraub AS, Li CH, Zamudio AV, Sigova AA, Hannett NM, Day DS, *et al.* YY1 is a structural regulator of enhancer-promoter loops. *Cell* 2017;171:1573–1588.e28. https://doi.org/10.1016/j.cell.2017.11.008.
51. Jin J, Wang K, Lu C, Yao C, Xie F. YY1-induced long noncoding RNA HOXA11-AS activates oxidative stress and inflammation by epigenetic modification of Nrf2 pathway to promote keloid formation. *Redox Rep Commun Free Radic Res* 2025;30:2539030. https://doi.org/10.1080/13510002.2025.2539030.
52. Yang T, Shu F, Yang H, Heng C, Zhou Y, Chen Y, *et al.* YY1: a novel therapeutic target for diabetic nephropathy orchestrated renal fibrosis. *Metabolism* 2019;96:33–45. https://doi.org/10.1016/j.metabol.2019.04.013.
53. Chen L, Yang Y, Peng X, Yan H, Zhang X, Yin L, *et al.* Transcription factor YY1 inhibits the expression of THY1 to promote interstitial pulmonary fibrosis by activating the HSF1/miR-214 axis. *Aging* 2020;12:8339–51. https://doi.org/10.18632/aging.103142.
54. Tan CY, Wong JX, Chan PS, Tan H, Liao D, Chen W, *et al.* Yin Yang 1 suppresses dilated cardiomyopathy and cardiac fibrosis through regulation of Bmp7 and Ctgf. *Circ Res* 2019;125:834–46. https://doi.org/10.1161/CIRCRESAHA.119.314794.
55. Huang Y, Li L, Chen H, Liao Q, Yang X, Yang D, *et al.* The protective role of Yin-Yang 1 in cardiac injury and Remodeling after myocardial infarction. *J Am Heart Assoc* 2021;10:e021895. https://doi.org/10.1161/JAHA.121.021895.
56. Hu X, Xu Q, Wan H, Hu Y, Xing S, Yang H, *et al.* PI3K-Akt-mTOR/PFKFB3 pathway mediated lung fibroblast aerobic glycolysis and collagen synthesis in lipopolysaccharide-induced pulmonary fibrosis. *Lab Investig J Tech Methods Pathol* 2020;100:801–11. https://doi.org/10.1038/s41374-020-0404-9.
57. Liu M, Ning X, Li R, Yang Z, Yang X, Sun S, *et al.* Signalling pathways involved in hypoxia-induced renal fibrosis. *J Cell Mol Med* 2017;21:1248–59. https://doi.org/10.1111/jcmm.13060.
58. Wu L, Zhang Q, Mo W, Feng J, Li S, Li J, *et al.* Quercetin prevents hepatic fibrosis by inhibiting hepatic stellate cell activation and reducing autophagy via the TGF-β1/Smads and PI3K/Akt pathways. *Sci Rep* 2017;7:9289. https://doi.org/10.1038/s41598-017-09673-5.
59. Xu Y, Wang X, Han D, Wang J, Luo Z, Jin T, *et al.* Revealing the mechanism of Jiegeng decoction attenuates bleomycin-induced pulmonary fibrosis via PI3K/Akt signaling pathway based on lipidomics and transcriptomics. *Phytomed Int J Phytother Phytopharm* 2022;102:154207. https://doi.org/10.1016/j.phymed.2022.154207.
60. Zhang Q, Wang L, Wang S, Cheng H, Xu L, Pei G, *et al.* Signaling pathways and targeted therapy for myocardial infarction. *Signal Transduct Target Ther* 2022;7:78. https://doi.org/10.1038/s41392-022-00925-z.
61. Liu J, Yan J, Qi S, Zhang J, Zhang X, Zhao Y. The PI3K/AKT/mTOR pathway in scar remodeling and keloid formation: mechanisms and therapeutic perspectives. *Front Pharmacol* 2025;16:1678953. https://doi.org/10.3389/fphar.2025.1678953.
62. Hays E, Bonavida B. YY1 regulates cancer cell immune resistance by modulating PD-L1 expression. *Drug Resist Updat Rev Comment Antimicrob Anticancer Chemother* 2019;43:10–28. https://doi.org/10.1016/j.drup.2019.04.001.
63. Yang P, Li J, Peng C, Tan Y, Chen R, Peng W, *et al.* TCONS_00012883 promotes proliferation and metastasis

Downloaded from academic.oup.com/burnstrauma/article/doi/10.1093/burnst/tkag027/8571429 by guest on 12 October 2026

via DDX3/YY1/MMP1/PI3K-AKT axis in colorectal cancer. *Clin Transl Med* 2020;10:e211. https://doi.org/10.1002/ctm2.211.

64. Zhou S, Qu KL, Li JA, Chen SL, Zhang YG, Zhu C, *et al.* YY1 activates EMI2 and promotes the progression of cholangiocarcinoma through the PI3K/Akt signaling axis. *Cancer Cell Int* 2021;21:699. https://doi.org/10.1186/s12935-021-02328-6.
65. Song Y, Guo B, Ma S, Chang P, Tao K. Naringin suppresses the growth and motility of hypertrophic scar fibroblasts by inhibiting the kinase activity of Akt. *Biomed Pharmacother* 2018;105:1291–8. https://doi.org/10.1016/j.biopha.2018.06.103.
66. Wu X, Wang Z, Wu G, Xu X, Zhang J, Li Y, *et al.* Tetramethylpyrazine induces apoptosis and inhibits proliferation of hypertrophic scar-derived fibroblasts via inhibiting the phosphorylation of AKT. *Front Pharmacol* 2020;11:602. https://doi.org/10.3389/fphar.2020.00602.
67. Li Y, Zhang J, Zhou Q, Wang H, Xie S, Yang X, *et al.* Linagliptin inhibits high glucose-induced transdifferentiation of hypertrophic scar-derived fibroblasts to myofibroblasts via IGF/Akt/mTOR signalling pathway. *Exp Dermatol* 2019;28:19–27. https://doi.org/10.1111/exd.13800.
68. Pi Z, Qiu X, Liu J, Shi Y, Zeng Z, Xiao R. Activating Protein-1 (AP-1): a promising target for the treatment of fibrotic diseases. *Curr Med Chem* 2023;31:904–18. https://doi.org/10.2174/0929867330666230209100059.
69. Dulauroy S, Di Carlo SE, Langa F, Eberl G, Peduto L. Lineage tracing and genetic ablation of ADAM12(+) perivascular cells identify a major source of profibrotic cells during acute tissue injury. *Nat Med* 2012;18:1262–70. https://doi.org/10.1038/nm.2848.
70. Crawford J, Nygard K, Gan BS, O'Gorman DB. Periostin induces fibroblast proliferation and myofibroblast persistence in hypertrophic scarring. *Exp Dermatol* 2015;24:120–6. https://doi.org/10.1111/exd.12601.
71. Yokota K, Kobayakawa K, Saito T, Hara M, Kijima K, Ohkawa Y, *et al.* Periostin promotes scar formation through the interaction between Pericytes and infiltrating monocytes/macrophages after spinal cord injury. *Am J Pathol* 2017;187:639–53. https://doi.org/10.1016/j.ajpath.2016.11.010.
72. Jeon KI, Nehrke K, Huxlin KR. Semaphorin 3A potentiates the profibrotic effects of transforming growth factor-β1 in the cornea. *Biochem Biophys Res Commun* 2020;521:333–9. https://doi.org/10.1016/j.bbrc.2019.10.107.
73. De Angelis Rigotti F, Wiedmann L, Hubert MO, Vacca M, Hasan SS, Moll I, *et al.* Semaphorin 3C exacerbates liver fibrosis. *Hepatol Baltim Md* 2023;78:1092–105. https://doi.org/10.1097/HEP.0000000000000407.

Downloaded from academic.oup.com/burnstrauma/article/doi/10.1093/burnst/tkag027/8571429 by guest on 12 October 2026

© The Author(s) 2026. Published by Oxford University Press. This is an Open Access article distributed under the terms of the Creative Commons Attribution-NonCommercial License (https://creativecommons.org/licenses/by-nc/4.0/), which permits non-commercial re-use, distribution, and reproduction in any medium, provided the original work is properly cited. For commercial re-use, please contact reprints@oup.com for reprints and translation rights for reprints. All other permissions can be obtained through our RightsLink service via the Permissions link on the article page on our site—for further information please contact journals.permissions@oup.com.
Burns & Trauma, 2026, 14, tkag027
https://doi.org/10.1093/burnst/tkag027
Research Article